

BEHAVIOR OF FINITE VOLUME SCHEMES FOR HYPERBOLIC CONSERVATION LAWS ON ADAPTIVE REDISTRIBUTED SPATIAL GRIDS*

CH. ARVANITIS[†] AND A. I. DELIS[‡]

Abstract. In this work we consider finite volume schemes combined with dynamic spatial mesh redistribution. We study whether appropriate mesh redistribution is a satisfactory mechanism for increasing the resolution of numerical solutions for problems of scalar and systems of conservation laws (CL) in one space dimension, while being at the same time a stabilization mechanism for selecting the appropriate entropy solution. In order to increase the resolution around shock areas and keep the computational cost low, our redistribution policy is to reconstruct spatially the numerical solution on a new mesh, where the solution's curvature is almost uniformly distributed, while the node's cardinality is kept constant. We examine the stabilization properties of that redistribution process by adding it as a substep on the time evolution step of some classical schemes with known (unstable) characteristics. Testing the resulting method for several such schemes and on a large number of CL problems that have solutions with special characteristics (shocks, rarefaction areas, steady states) and comparing the results with those produced by schemes with extra stabilization mechanisms (like slope/flux limiters, entropy corrections), we conclude that indeed the proposed redistribution adds such stabilization properties while at the same time increasing the resolution.

Key words. finite volume methods, adaptive grid redistribution, hyperbolic conservation laws

AMS subject classifications. 35L65, 76M12, 65M12

DOI. 10.1137/050632853

1. Introduction. The application of finite volume schemes is a very popular choice for computing solutions of systems of conservation laws (CL) in the following context: *find* $u : \mathbb{R}^d \times [0, T] \rightarrow \mathbb{R}^M$ such that

$$(1.1) \quad \begin{aligned} u(\cdot, 0) &= u_0 \quad \text{given} \\ \partial_t u + \sum_{i=1}^d \partial_{x_i} F_i(u) &= 0. \end{aligned}$$

Some classical schemes, of first or second order in space, when applied directly to this system will result in computational solutions with diffusive or oscillatory behavior, especially close to shocks. To overcome this difficulty several modifications of such schemes have been proposed in the literature where the necessary stability and viscosity mechanisms are imposed “by hand.” Mesh adaptation is a main current stream to efficiently compute numerical solutions of complex systems by increasing the resolution of the essential solution. Several redistribution techniques have been introduced recently for solving the problem of proper mesh selection, starting with the self-adjusting method of Harten and Hyman [14] to the moving mesh methods of Azarenok et al., Fazio and LeVeque, Stockie et al., Tao Tang, Huazhong Tang, and

*Received by the editors June 1, 2005; accepted for publication (in revised form) May 15, 2006; published electronically November 16, 2006.

<http://www.siam.org/journals/sisc/28-5/63285.html>

[†]Department of Applied Mathematics, University of Crete, Heraklion 71409, Crete, Greece (arvas@tem.uoc.gr). The work of this author was partially supported by the European Union RTN-network HYKE, HPRN-CT-2002-00282, and the program Pythagoras of EPEAEK II.

[‡]Department of Sciences, Division of Mathematics, Technical University of Crete, University Campus, Chania 73100, Crete, Greece (adelis@science.tuc.gr).

others (see [4], [5], [6], [8], [12], [17], [19], [20], [21], [23], [27], [28], [29], [30]). These methods calculate the spatial positions of the nodes of the new mesh, some of them by solving an Euler–Lagrange equation, others by optimizing proper energy metrics. All of them have as a common factor that they can be combined with any numerical scheme (making appropriate modifications) for increasing its resolution.

In this work the evolving mesh is constructed such that its spatial resolution is controlled via selective characteristics of the computed solution. Our main aim here is to experimentally study the behavior of finite difference–volume schemes, with or without stabilization mechanisms, but under the regime of this adaptively evolving mesh. Our choice of classical schemes includes, for example, the first order Roe scheme, the second order Lax–Wendroff and MacCormack schemes, and also some TVD schemes. The adaptive procedure studied in this work is based on a mesh redistribution policy that evolves within every computational time step. The basic principle of the suggested mesh redistribution is to (re)distribute the nodes of the generated partition with respect to geometrical characteristics of the solution. These characteristics are defined through a positive functional of the solution, the so-called *estimator function* [1], [2], [3]. Among other estimator functions for evolution PDEs, like the arc-length and variance, we choose the curvature of the solution as such a function, for its diffuseless behavior. Experiments in [3] with Galerkin finite element schemes, which approximate CL solutions like central finite difference schemes, have shown that this redistribution procedure has stabilization properties of its own. For example, in this work we show that schemes like Lax–Wendroff combined with our redistribution policy provide surprisingly stable solutions free of oscillations. From the numerical experiments produced in the course of this work we concluded the following advantages of the use of this particular adaptive grid redistribution (AGR) method.

- The method when applied to classical second order schemes, which produce oscillating solutions, suppresses the oscillations, producing TVD-like approximations. Classical schemes like the Lax–Wendroff or the MacCormack scheme become stable and produce reliable solutions.
- When applied to numerical schemes that do not satisfy entropy conditions, for example, the original Roe scheme, the method approximates the entropy satisfying solution.
- The method works well for hyperbolic problems with source terms and produces stable solutions for first and second order balanced schemes and can converge to correct steady states.
- The method can automatically detect, resolve, and track steep wave fronts and discontinuities, without having to resort to finer grids.
- The AGR method is of linear complexity, as we will see in the next section (cf. Remark 3), and consequently its computational cost is in favor when compared, for example, to the stabilization mechanisms for high resolution TVD schemes, where we have to solve a number of Riemann problems in order to compute the corresponding stabilization limiters.
- The mechanism has been proved robust for all the applications presented and schemes used.

Following from the above, our main conclusion from the present work is that numerical schemes, when combined with the proposed mesh adaptation, yield stable solutions free of oscillations.

The paper is organized as follows. In the next section we define the AGR algorithm. In section 3 we present finite volume schemes for scalar CL, adjusted to nonuniform grids, which will be tested in the regime of the adaptive redistribution al-

gorithm. Section 4 is devoted to numerical results. In section 5 numerical schemes for systems of CL, with or without source terms, are detailed, and in section 6 numerical results for the shallow water system of equations are presented.

2. The AGR method in one dimension. Let X be a partition of a domain $[a, b]$ and $\{x_i\}_{i=0}^N$ the corresponding nodes in increasing order, i.e., $a = x_0 < x_1 < \dots < x_{N-1} < x_N = b$. Then we introduce the following notation:

- With $\sigma(X)$ we denote the σ -algebra of X , which for finite partitions coincides with the superset of unions of sets from X .
- With **resolution** of X , we denote the measure which for any measurable set A is defined by

$$\text{resolution}(A) = \text{card}\{K \in X : K \subset A\},$$

i.e., the resolution of the partition X over some set A is the number of partition elements that A contains.

- If $U = \{u_i\}_{i=0}^N$ is a vector of values defined on elements of the partition X , then it shall be notated as $U(X)$. For compatibility with approximations given from finite volume schemes, in the following we shall identify any vector of function values $\{u_i\}_{i=0}^N$ evaluated on partition nodes $\{x_i\}_{i=0}^N$, i.e., $U = U(X)$, with the locally constant function U , defined on $[a, b]$ by

$$(2.1) \quad U = \sum_{i=0}^N u_i \chi_{[x_{i-1}^+, x_i^+)} + u_N \chi_{\{x_N^+\}},$$

with χ_A denoting the characteristic function of the set A , and $\{x_i^+\}_{i=-1}^N$ denoting the points

$$x_{-1}^+ = x_0, \quad x_i^+ = x_{i+\frac{1}{2}}, \quad i = 0, 1, \dots, N-1, \quad x_N^+ = x_N.$$

In the case of evolution PDEs, where the numerical solution is constructed like a sequence of spatial approximations of solutions instances, the redistribution process could be applied before every evolution step. Let **Solver** denote a (general) finite volume scheme for solving some evolution PDE. For $n = 1, 2, \dots$ **Solver** gives sequentially the approximations U^n of the solution instances $u(t^n, \cdot)$ at given time moments $t^0 < t^1 < \dots < t^n \in \mathbb{R}^+$, starting at $t^0 = 0$. The given initial data U^0 is defined on the uniform partition X^0 of the domain. In the case of uniform partition, the evolution step can be represented for $n = 1, 2, \dots$ as an equation on the vector space $\mathbb{R}^{2(N+1)}$:

$$(X^n, U^n(X^n)) = (X^{n-1}, \text{Solver}(X^{n-1}, U^{n-1}(X^{n-1}))).$$

On meshes generated by the AGR process, the evolution step can be represented by the system of vector equations:

$$(2.2) \quad \begin{aligned} (\tilde{X}, \tilde{U}(\tilde{X})) &= \text{AGR}(X^{n-1}, U^{n-1}(X^{n-1})), \\ (X^n, U^n(X^n)) &= (\tilde{X}, \text{Solver}(\tilde{X}, \tilde{U}(\tilde{X}))), \end{aligned}$$

where \tilde{X}, \tilde{U} are temporal vectors. Observe that in the case where the AGR process returns the same vectors, i.e., the AGR coincides with the identity linear transformation, then (2.2) reduces to the uniform evolution step. The AGR procedure, for a

given vector of values $U = \{u_i\}_{i=0}^N$ defined on the nodes $\{x_i\}_{i=0}^N$ of the partition X , i.e., $U = U(X)$, is described by the following two sequential steps,

$$(2.3) \quad \begin{aligned} \tilde{X} &= \mathbf{GMesh}(X, U(X)), \\ \tilde{U}(\tilde{X}) &= \mathbf{Rec}(X, U(X), \tilde{X}). \end{aligned}$$

In what follows we describe in detail the two steps **GMesh**, **Rec** of our redistribution algorithm AGR.

2.1. The GMesh step. At the **GMesh** step of the AGR procedure (2.3), a new partition \tilde{X} of spatial nodes $\{\tilde{x}_i\}_{i=0}^N$ is formed, with resolution controlled by selected characteristics of the numerical solution U . The step is accomplished in two phases.

At the *first phase* the selected characteristics are defined on the domain $[a, b]$ through a strictly positive functional g of the approximate solution, the *estimator function*. Since we are mainly interested in increasing the resolution over areas with discontinuities, and taking into account the results in [3], in this work we will also use some power p of proper approximation of the solution’s curvature defined by

$$(\text{curv} \circ u)(x) = \frac{|u''(x)|}{(1 + u'(x)^2)^{\frac{3}{2}}}$$

as the estimator function for selecting the resolution’s density of the new partition. For a given partition $\{x_i\}_{i=0}^N$, the solution’s curvature at the node x_i can be approximated by

$$(\text{curv}_h \circ u)(x_i) = \frac{\frac{2}{x_{i+1}-x_{i-1}} \left| \frac{u(x_i)-u(x_{i-1})}{x_i-x_{i-1}} - \frac{u(x_{i+1})-u(x_i)}{x_{i+1}-x_i} \right|}{\sqrt{1 + \left(\frac{u(x_i)-u(x_{i-1})}{x_i-x_{i-1}}\right)^2} \sqrt{1 + \left(\frac{u(x_{i+1})-u(x_i)}{x_{i+1}-x_i}\right)^2} \sqrt{1 + \left(\frac{u(x_{i+1})-u(x_{i-1})}{x_{i+1}-x_{i-1}}\right)^2}},$$

which is the inverse outer radius of the plane points $A_j = (x_j, u(x_j))$, $j = i - 1, i, i + 1$, i.e.,

$$(\text{curv}_h \circ u)(x_i) = 2 \frac{\|(A_{i+1} - A_i) \times (A_i - A_{i-1})\|}{\|A_{i+1} - A_i\| \|A_{i+1} - A_{i-1}\| \|A_i - A_{i-1}\|},$$

where $\|\cdot\|$ denotes the Euclidean norm. Thus, at the discrete level, the values g_i of our estimator function on the node points $\{x_i\}_{i=0}^N$, are given by $g_0 = g_N = \delta^p$ and for $i = 1, \dots, N - 1$,

$$(2.4) \quad g_i = \left(\max \left\{ \delta, 2 \frac{\|(A_{i+1} - A_i) \times (A_i - A_{i-1})\|}{\|A_{i+1} - A_i\| \|A_{i+1} - A_{i-1}\| \|A_i - A_{i-1}\|} \right\} \right)^p,$$

where the power p is left as a free parameter taking values in the range $[0, 1]$ and δ is a very small positive number which ensures that g_i is strictly positive. The constant δ must be chosen such that, at a computational level, g_i behaves monotonically as a function of p even for negligible values. In our experiments, where the calculations were performed with ANSI-C computational libraries of double precision, δ was fixed to the value 10^{-32} . In the case of vector solution $u = (u_1, \dots, u_M)^T$, we intend to use the average of the coordinate estimators as the uniform estimator function for all the coordinates of the solution. Therefore, in general, instead of the values g_i we keep the normalized version $g_i / \sum_{j=0}^N g_j$, $i = 0, 1, \dots, N$.

At the *second phase*, the partition \tilde{X} is actually produced through $g_h \circ U$, the corresponding function of type (2.1) to values (2.4). Since we expect a new mesh \tilde{X} with resolution that locally follows the function $g_h \circ U$, we conclude that the resolution measure must be distributed in space like the measure $G_U(A) = \int_A (g_h \circ U) d\mu$ introduced by the positive function $g_h \circ U$, at least for sets from $\sigma(\tilde{X})$. Therefore the new partition \tilde{X} is defined such that

$$(2.5) \quad \forall A \in \sigma(\tilde{X}) \quad G_U(A) = C \text{ resolution}(A), \text{ with } C = \frac{G_U([a, b])}{N}.$$

Applying sequentially (2.5) with the sets $A_i = [a, \tilde{x}_i]$, $i = 1, 2, \dots, N$, where their indices declare also the resolution of the partition \tilde{X} over them, we induce, as it is called in the literature of moving meshes, the *equidistribution principal*:

$$(2.6) \quad \tilde{x}_0 = a \text{ and for } i = 1, \dots, N, \tilde{x}_i \text{ is such that } \int_a^{\tilde{x}_i} g_h(U(x)) dx = \frac{i}{N} \int_a^b g_h(U(x)) dx.$$

In the present work, the new mesh \tilde{X} is defined through (2.6), but we note that other inverting algorithms could also be constructed through a more elegant treatment of the generic equidistribution principal (2.5). Let $G(x) = G_U([a, x])$ be the distribution function, which is an increasing local linear function defined on the grid X , since $g_h \circ U$ is a positive function of type (2.1). Thus, G is completely defined from the values $G_i = G(x_i)$ of the G_U measure of the intervals $[a, x_i]$, that is, $G_0 = 0$, and for $i = 1, \dots, N$,

$$(2.7) \quad G_i = G_U([a, x_i]) = \int_{[a, x_i]} (g_h \circ U) d\mu = G_{i-1} + \int_{x_{i-1}}^{x_i} g_h(U(x)) dx$$

$$\stackrel{(2.1)}{=} G_{i-1} + (g_{i-1} + g_i)(x_i - x_{i-1})/2.$$

From (2.6) it follows that the \tilde{x}_i node is given by inverting the equation $G(\tilde{x}_i) = \frac{i}{N}G(\tilde{x}_N)$, so the nodes of the new mesh \tilde{X} are $\tilde{x}_0 = a$, $\tilde{x}_N = b$, and, for $i = 1, \dots, N-1$, $k_0 := 0$,

$$(2.8) \quad \tilde{G}_i = \frac{i}{N}G_N, \quad k_i = \max_{k_{i-1} \leq \ell \leq N} \{ \ell : G_\ell \leq \tilde{G}_i \}, \quad \tilde{x}_i = x_{k_i} + \frac{x_{k_{i+1}} - x_{k_i}}{G_{k_{i+1}} - G_{k_i}} (\tilde{G}_i - G_{k_i}).$$

2.2. The Rec step. At the **Rec** step of the AGR procedure (2.3), a new numerical solution $\tilde{U} = \{\tilde{u}_i\}_{i=0}^N$ of type (2.1) is defined on the new grid \tilde{X} by reconstructing U from the old grid X to the new one. Since the schemes used in this work produce conservative solutions, the reconstruction step is done so that it is locally conservative on each interval $[\tilde{x}_{i-1}^+, \tilde{x}_i^+]$ of the new mesh. That is, for $i = 0, \dots, N$, we require

$$\int_{\tilde{x}_{i-1}^+}^{\tilde{x}_i^+} \tilde{U}(x) dx = \int_{\tilde{x}_{i-1}^+}^{\tilde{x}_i^+} U(x) dx.$$

Since the functions U, \tilde{U} are of type (2.1) defined on the partitions X, \tilde{X} , respectively,

$$\tilde{u}_i(\tilde{x}_i^+ - \tilde{x}_{i-1}^+) = \int_{\tilde{x}_{i-1}^+}^{\tilde{x}_i^+} U(x) dx = \int_{x_{k_i}^+}^{\tilde{x}_i^+} U(x) dx + \int_{x_{k_i}^+}^{x_{k_{i+1}}^+} U(x) dx - \int_{x_{k_{i-1}}^+}^{\tilde{x}_{i-1}^+} U(x) dx,$$

where, using the real line ordering of the domain $[a, b]$, $x_{k_i}^+$ denotes the larger node from the old partition not exceeding the node \tilde{x}_i^+ of the new partition. Consequently, the new values \tilde{U} are $\tilde{u}_0 = u_0$ and, for $i = 1, \dots, N$, $k_0 := 0$,

$$(2.9) \quad k_i = \max_{k_{i-1} \leq \ell \leq N} \{ \ell : x_\ell^+ \leq \tilde{x}_i^+ \},$$

$$\tilde{u}_i = \left\{ (\tilde{x}_i^+ - x_{k_i}^+) u_{k_i+1} + \sum_{\ell=k_{i-1}+1}^{k_i} (x_\ell^+ - x_{\ell-1}^+) u_\ell - (\tilde{x}_{i-1}^+ - x_{k_{i-1}}^+) u_{k_{i-1}+1} \right\} / (\tilde{x}_i^+ - \tilde{x}_{i-1}^+).$$

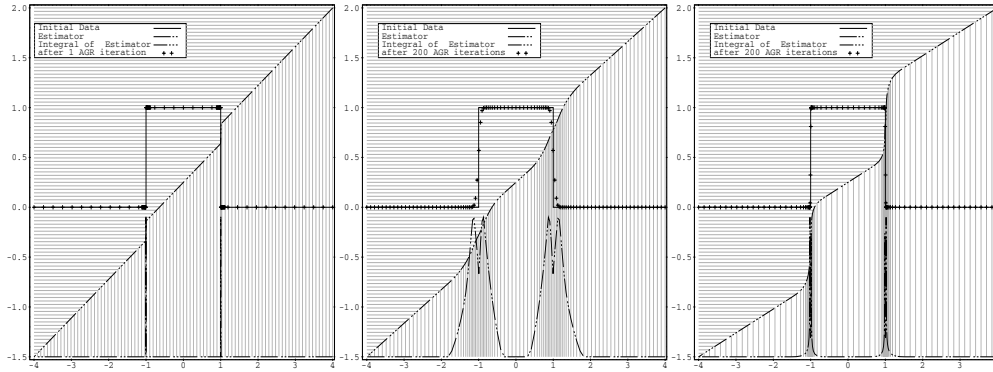


FIG. 1. Iteration of the AGR procedure applied on Riemann data. After 1 iteration (left) and after 200 iterations for $p = 0.023$ (middle) and $p = 0.1$ (right).

The **Gmesh** step of the AGR process can be graphically represented as in Figure 1. Starting with some initial data (solid line) we calculate the estimator function (dotted line) through (2.4) and then the corresponding distribution function (increasing dotted line) using (2.7). The proposed mesh (x position of the vertical lines, under the distribution function) is given by inverting a uniform mesh (y position of the horizontal lines, over the distribution function) through the distribution function using (2.8). Notice that y -coordinates are valid only for the data while either the estimator or its distribution function was scaled vertically to fit on the viewing graph area.

Remark 1 (the action of the parameter p). Parameter p controls essentially the maximum density of the generated mesh \tilde{X} . Indeed, from relations (2.4), (2.6), we conclude that the corresponding nodes \tilde{x}_i , $i = 1, \dots, N$, satisfy the equation

$$\frac{1}{N} \int_a^b \text{curv}_h^p(U(x)) \, dx = \int_{\tilde{x}_{i-1}}^{\tilde{x}_i} \text{curv}_h^p(U(x)) \, dx \leq \max_{x \in [\tilde{x}_{i-1}, \tilde{x}_i]} \{ \text{curv}_h^p(U(x)) \} (\tilde{x}_i - \tilde{x}_{i-1}),$$

and therefore

$$\frac{1}{N} \left(\frac{\| \text{curv}_h \circ U \|_{L^p[a,b]}}{\| \text{curv}_h \circ U \|_{L^\infty[a,b]}} \right)^p \leq \min_i \{ \tilde{x}_i - \tilde{x}_{i-1} \}.$$

Thus, choosing p appropriately, the resolution of the \tilde{X} mesh respects an upper given bound. The action of the parameter p in the AGR procedure can also be seen in

Figure 1 (middle, right). For $p = 0$ observe from (2.7) that $G_i = x_i - x_0$, so the proposed partition from (2.8) coincides with the uniform partition of $[a, b]$. As the value of p increases, the proposed partition becomes more dense on the discontinuity areas, but over some value of p the process becomes unreliable because the partition lacks nodes over smooth areas. In our experiments with finite volume schemes an appropriate range for the parameter p was $[0.02, 0.10]$ for first order and $[0.04, 0.14]$ for second order schemes.

Remark 2 (smoothing effect of the AGR process). Results in [3] show that the reconstructed function \tilde{U} of the AGR procedure is more diffusive than the initial function U . Indeed this diffusive behavior can be observed by applying the AGR procedure iteratively on some initial data, i.e., starting with some initial data U^0 on the uniform partition X^0 of $[a, b]$, we define the sequence $(X^n, U^n(X^n)) = \mathbf{AGR}(X^{n-1}, U^{n-1}(X^{n-1}))$, $n = 1, 2, \dots$. Experiments with Riemann initial data show that the above sequence attains a limit pair $(X, U(X))$. In Figure 1 (middle, right) we present the results after 200 iterations for $p = 0.023$ (middle) and for $p = 0.1$ (right). In Figure 2 (middle, right) we present the trajectories of the nodes for the above iterative process. Notice that after about 20 iterations for $p = 0.023$ and about 80 for $p = 0.1$ the position of all the nodes X stabilizes. But from (2.9) one can observe that reconstructing any function on the same grid leads to the same function, i.e., $U(X) = \mathbf{Rec}(X, U(X), X)$, so we conclude that also the reconstructed values $U(X)$ after the above iterations became constant. Figure 2 (left) shows the smoothing effect of the AGR process on the initial data after 200 iterations and for various values of p .

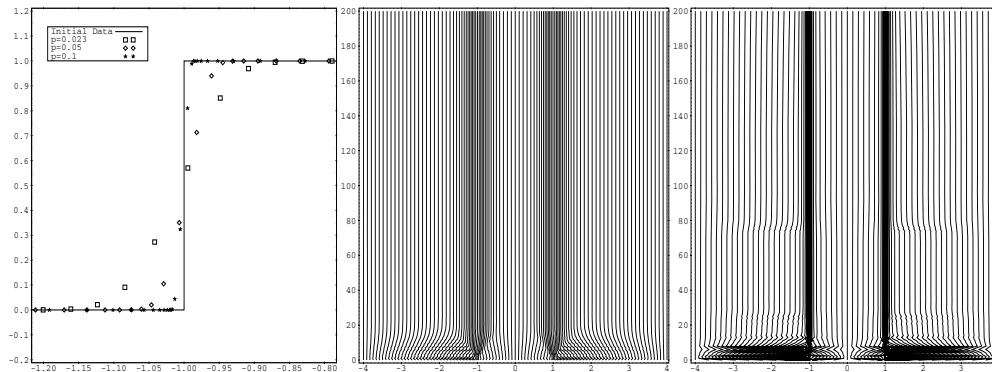


FIG. 2. Focus in the shock area (left) after 200 iterations of the AGR procedure and for various values of parameter p . Trajectories of mesh nodes for $p = 0.023$ (middle) and for $p = 0.1$ (right).

Remark 3 (complexity of the AGR process). Observe that both the **Gmesh** step (2.7), (2.8) and the **Rec** step (2.9) of the AGR process are of linear complexity.

2.3. Redistribution in the steady state regime. The diffusive behavior of the AGR process might be one of the reasons that second order schemes, when combined with the redistribution step, produce nonoscillatory approximations; however, in the case where the current and the new mesh are almost the same the redistribution step should be avoided. In addition, in the case of very sensitive CL problems with steady states we noticed that the repeated application of the AGR process prevents the conservation of the steady states. Taking into account these observations, in the numerical experiments of this work we adopt a new version of the AGR process:

$$\begin{aligned} \tilde{X} &= \mathbf{GMesh}(X, U), \\ \text{if } (|X - \tilde{X}| > D), \quad \tilde{U} &= \mathbf{Rec}(X, U, \tilde{X}), \\ \text{else} \quad \tilde{X} &= X, \quad \tilde{U} = U, \end{aligned}$$

where D is a “cutoff” level for the relative mean displacement $|X - \tilde{X}|$ between the current and the proposed meshes, under which the **Rec** step is avoided. The relative mean displacement is measured in the ℓ^1 vector norm, that is, $|X - \tilde{X}| = \frac{1}{N+1} \frac{\sum_{i=0}^N |x_i - \tilde{x}_i|}{b-a}$. Experiments show that, for first order schemes or those with extra stabilization mechanisms (like using slope/flux limiters), the AGR process produces results with higher resolution when the cutoff parameter D is of order 10^{-2} , whereas, due to the oscillatory behavior of second order schemes like the classical Lax–Wendroff, the cutoff level can be of order 10^{-3} or even less. In all cases, when the problem imposes steady states a nonzero value of D is crucial for the solving process in order to reach the time invariant solution for all schemes. The above observations become more pronounced for systems of conservation laws.

3. Numerical schemes on nonuniform grids (one-dimensional scalar equations). In this section we review some well-known classical numerical schemes, implemented at the **Solver** step, for the discretization of a scalar conservation law,

$$(3.1) \quad u_t + f(u)_x = 0,$$

and present them in their nonuniform grid formulation. We will also state some well-known disadvantages that these schemes exhibit.

We will approximate the solution $u(t, x)$, $x \in \mathbb{R}$, $t \geq 0$, of (3.1) by the discrete values u_i^n , $i \in \mathbb{Z}$, $n \in \mathbb{N}$, and in order to do so we consider a grid of points $x_{i+\frac{1}{2}}$ and define the computational cells and their lengths as

$$C_i = [x_{i-\frac{1}{2}}, x_{i+\frac{1}{2}}], \quad \Delta x_i = x_{i+\frac{1}{2}} - x_{i-\frac{1}{2}} > 0.$$

We also denote by $x_i = (x_{i-\frac{1}{2}} + x_{i+\frac{1}{2}})/2$ the centers of the partition cells. The values u_i^n will be approximations of the averages of the exact solution over the cell

$$u_i^n \approx \frac{1}{\Delta x_i} \int_{C_i} u(t^n, x) dx,$$

with t^n the discrete time levels.

For consistency, we present the schemes in the usual conservative formulation with explicit time stepping,

$$(3.2) \quad u_i^{n+1} = u_i^n - \frac{\Delta t}{\Delta x_i} \left(f_{i+\frac{1}{2}}^n - f_{i-\frac{1}{2}}^n \right),$$

where $f_{i+\frac{1}{2}}^n$, $i = 1, 2, \dots, N-1$, is the numerical flux function that determines the scheme.

First order Roe scheme. The numerical flux of the well-known first order upwind Roe scheme is given by (see [15])

$$(3.3) \quad f_{i+\frac{1}{2}}^{\text{ROE}} = \frac{1}{2} \left(f_{i+1} + f_i - |a_{i+\frac{1}{2}}| \Delta u_{i+\frac{1}{2}} \right),$$

with $f_i = f(u_i)$, $\Delta u_{i+\frac{1}{2}} = u_{i+1} - u_i$ and $|a_{i+\frac{1}{2}}|$ the characteristic speed defined by

$$(3.4) \quad a_{i+\frac{1}{2}} = \begin{cases} \frac{f_{i+1} - f_i}{u_{i+1} - u_i}, & u_{i+1} \neq u_i, \\ a_i = \frac{\partial f}{\partial u}, & u_{i+1} = u_i. \end{cases}$$

A well-known drawback of Roe's scheme is that it may resolve nonphysical solutions by admitting stationary entropy-violating expansion shocks. Various *entropy corrections* have been proposed; see [18]. For example, we can replace the moduli of a in (3.3) by

$$\psi(a) = \max(\delta, |a|)$$

or by the smoother form

$$\psi(a) = \begin{cases} |a|, & |a| \geq \delta, \\ (a^2 + \delta^2)/2\delta, & |a| < \delta, \end{cases}$$

with

$$\delta_{i+\frac{1}{2}} = \max\{0, a_{i+\frac{1}{2}} - a_i, a_{i+1} - a_{i+\frac{1}{2}}\}, \quad \delta_{i-\frac{1}{2}} = \max\{0, a_{i-\frac{1}{2}} - a_{i-1}, a_i - a_{i-\frac{1}{2}}\}.$$

The Roe numerical flux is then defined as

$$(3.5) \quad f_{i+\frac{1}{2}}^{\text{ROE}} = \frac{1}{2} \left(f_{i+1} + f_i - \psi(a_{i+\frac{1}{2}}) \Delta u_{i+\frac{1}{2}} \right).$$

In our numerical examples to follow we will see that when the adaptive mechanism is applied, the above entropy corrections are not necessary for the scheme to produce approximations of entropy solutions. This is a first order diffusive scheme, but it serves as a key ingredient in developing higher order methods.

The local Lax-Friedrichs scheme. A well-known first order scheme that produces approximations of entropy solutions is the local Lax-Friedrichs (LF) scheme. Its numerical flux function (see [18]) is given by

$$(3.6) \quad f_{i+\frac{1}{2}}^{\text{LF}} = \frac{1}{2} \left(f_{i+1} + f_i - a_{\max} \Delta u_{i+\frac{1}{2}} \right),$$

where $a_{\max} = \max\{|f'(u_i)|, |f'(u_{i+1})|\}$. This scheme produces diffusive numerical solutions and smears discontinuities and was used for comparison reasons only.

The Lax-Wendroff scheme. A natural generalization of the classical second order Lax-Wendroff (LW) scheme for nonuniform grids can be given as a combination of the first order Roe flux plus a correction flux (see [18]):

$$(3.7) \quad f_{i+\frac{1}{2}}^{\text{LW}} = f_{i+\frac{1}{2}}^{\text{ROE}} + \frac{1}{2} \left(\frac{\Delta x_i}{0.5(\Delta x_{i+1} + \Delta x_i)} - \frac{\Delta t}{0.5(\Delta x_{i+1} + \Delta x_i)} |a_{i+\frac{1}{2}}| \right) |a_{i+\frac{1}{2}}| \Delta u_{i+\frac{1}{2}},$$

with $a_{i+\frac{1}{2}}$ as defined in (3.4). It is easy to see that for a uniform grid numerical flux (3.7) is reduced to the classical LW numerical flux. As for uniform grids this scheme has highly oscillatory behavior near discontinuities and without entropy correction cannot produce entropy solutions.

The MacCormack scheme. One of the most classical second order schemes (see [15]) is the well-known two-step MacCormack scheme:

$$(3.8) \quad u_i^{(1)} = u_i^n - \frac{\Delta t}{\Delta x_i} (f_{i+1}^n - f_i^n),$$

$$(3.9) \quad u_i^{(2)} = u_i^n - \frac{\Delta t}{\Delta x_i} (f_{i+1}^{(1)} - f_i^{(1)}),$$

$$(3.10) \quad u_i^{n+1} = \frac{1}{2} (u_i^{(1)} + u_i^{(2)}).$$

This simple scheme also exhibits oscillatory behavior near discontinuities and cannot produce the correct entropy solutions.

The MUSCL-TVD scheme. Here we present a second order slope-limiting scheme based on the MUSCL-TVD interpolation formula on nonuniform grids; see, for example, [22]. We define

$$u_{i+\frac{1}{2}}^L = u_i + \frac{h_{i+1}}{2} \left(\frac{u_i - u_{i-1}}{h_i} \right) \Phi(\theta_i),$$

$$u_{i+\frac{1}{2}}^R = u_{i+1} - \frac{h_{i+1}}{2} \left(\frac{u_{i+2} - u_{i+1}}{h_{i+2}} \right) \Phi\left(\frac{1}{\theta_{i+1}}\right),$$

with $h_i = x_i - x_{i-1}$ and θ_i given by

$$\theta_i = \frac{(u_{i+1} - u_i)/h_{i+1}}{(u_i - u_{i-1})/h_i}.$$

The Φ is a limiter function, and there are several options from which to choose Φ ; see, for example, [25]. Some of the most popular limiters are the MinMod (MM) limiter,

$$\Phi(\theta) = \max(0, \min(1, \theta)),$$

the Superbee (SB) limiter

$$\Phi(\theta) = \max(0, \min(2\theta, 1), \min(\theta, 2)),$$

the VanLeer (VL) limiter

$$\Phi(\theta) = \frac{|\theta| + \theta}{1 + |\theta|},$$

and the monotonized central (MC) limiter

$$\Phi(\theta) = \max(0, \min((1 + \theta)/2, 2, 2\theta)).$$

The numerical flux for the MUSCL scheme can then be expressed, based on the Roe flux (without an entropy fix), as

$$(3.11) \quad f_{i+\frac{1}{2}}^{\text{MUSCL}} = \frac{1}{2} \left(f(u_{i+\frac{1}{2}}^R) + f(u_{i+\frac{1}{2}}^L) - |a_{i+\frac{1}{2}}| (u_{i+\frac{1}{2}}^R - u_{i+\frac{1}{2}}^L) \right),$$

where $a_{i+\frac{1}{2}}$ is evaluated as before, with u_{i+1} and u_i replaced by $u_{i+\frac{1}{2}}^R$ and $u_{i+\frac{1}{2}}^L$. In a similar way one can define a MUSCL flux based on the LF flux.

Second order TVD schemes reduce to first order at extrema, and there are also differences in the behavior for each limiter; for example, the last three limiters have been shown to exhibit sharper resolution of discontinuities, since they do not reduce the slope as severely as MM near a discontinuity.

4. Numerical examples for scalar conservation laws. Because all the schemes presented above are explicit in time, stability requires the time step Δt to satisfy the CFL condition, as to ensure that the time step is small enough that waves from neighboring cells do not interact, with $\text{CFL} \leq 1$. Based on that we use a variable time step calculated from

$$(4.1) \quad \text{CFL} = \Delta t \max_i \left\{ \left| \frac{a_{i-\frac{1}{2}}^+}{\Delta x_i} \right|, \left| \frac{a_{i+\frac{1}{2}}^-}{\Delta x_i} \right| \right\},$$

with $a^+ = \max(0, a)$ and $a^- = \min(0, a)$.

4.1. Burgers equation. We first consider numerical experiments for the Burgers equation in the inviscid limit,

$$(4.2) \quad u_t + \left(\frac{u^2}{2} \right)_x = 0.$$

The analytical solutions to this problem can be found, for example, in [15].

The first problem is an academic test case with initial conditions, for $x \in [-5, 5]$,

$$(4.3) \quad u(x, 0) = \begin{cases} -1.0, & x < 0, \\ 1.0, & x \geq 0, \end{cases}$$

and has the following exact solution, also known as a *transonic rarefaction*:

$$(4.4) \quad u(x, 0) = \begin{cases} -1.0, & x < -t, \\ x/t, & -t \leq x \leq t, \\ 1.0, & x > t. \end{cases}$$

As pointed out in [18], dealing with transonic rarefactions properly is an important component in the development of successful methods. Results for this problem are presented in Figures 3 and 4 at $t = 2\text{s}$. A grid of 61 points was used for all schemes with CFL number equal to 0.9. All the schemes presented in the previous section, with the exception of the LF scheme, cannot produce the correct entropy solution. By the application of the adaptive mechanism all the schemes calculate the correct solution. The most accurate results were produced with the MUSCL adaptive scheme using the SB limiter. We note here that when the adaptive mechanism was applied to the MUSCL scheme, we were able to produce similar results for all limiters.

The second problem was presented in [22] and has initial conditions given by

$$(4.5) \quad u(x, 0) = \begin{cases} 1.0, & x \in [0.2, 2.0], \\ -0.5, & x \in (2.0, 3.0], \\ -1.0, & x \in (3.0, 4.8], \\ 0.0 & \text{otherwise.} \end{cases}$$

The solution domain is for $x \in [0, 5]$ with homogeneous Dirichlet conditions. This problem includes two shocks initially at $x = 2$ and $x = 3$, moving to the right and left, respectively, and two expansion discontinuities at $x = 0.2$ and $x = 4.8$ also expanding to the right and left, respectively. The two shocks collide at time $t = 1\text{s}$ and form a single shock moving to the left. The numerical results are presented in Figures 5 and 6 for $t = 2\text{s}$ when the shocks have combined into a single one. A grid of 121 points was used for all schemes with CFL number equal to 0.9. All the schemes

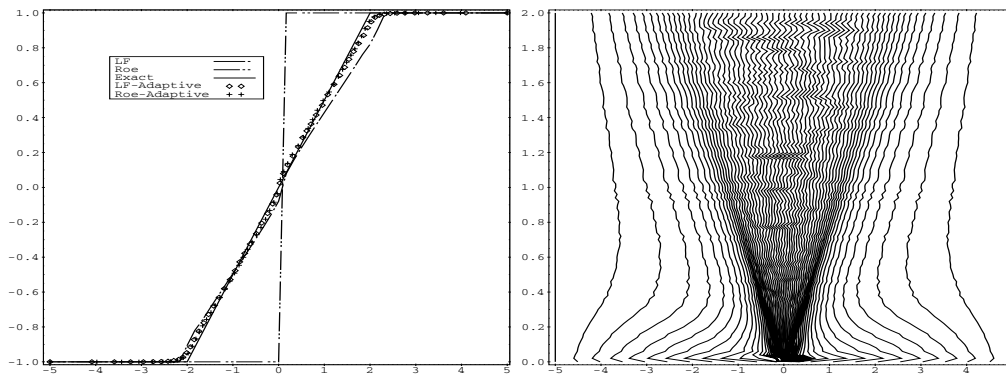


FIG. 3. Transonic rarefaction problem: Numerical solution (left) and grid point trajectories (right) for the adaptive Roe scheme ($p = 0.09$, $D = 0$).

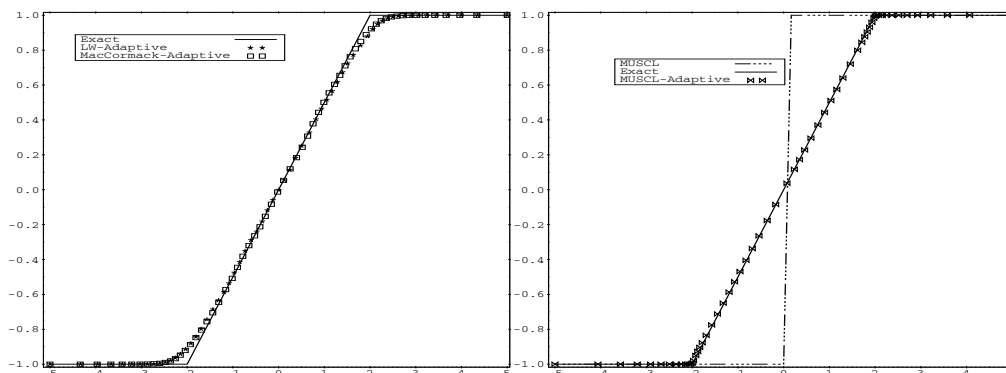


FIG. 4. Transonic rarefaction problem: Numerical solution (left) for the LW and MacCormack schemes ($p = 0.062$, $D = 0$) and (right) for the MUSCL scheme ($p = 0.10$, $D = 0$).

produce improved results when the adaptive mechanism is imposed, when compared to those produced in a uniform mesh. It is impressive that even the second order oscillatory LW and MacCormack schemes are now able to produce accurate solutions. The performance of the MUSCL using the MC limiter scheme is also greatly improved, since in the nonadaptive case the scheme fails to produce the entropy correct solution at expansions. Similar observations were made for the other limiters as well. In Figure 6 one can also see the ability of the mesh to capture and follow the evolution of the solution as demonstrated by the grid point trajectories.

The third problem has an initial profile of a smooth wave given by

$$u(x, 0) = 0.5 \sin(\pi x) + \sin(2\pi x), \quad x \in [0, 1],$$

with periodic boundary conditions imposed. The solution propagates to the right, steepening until the singularity time $t_c = 64/(129\pi)$. Results are presented in Figures 7 and 8 for the second order schemes for a 61-point grid and with a CFL number of 0.6 at $t = 1$ s, and verify the observations made for the second example. Considerably better results are obtained for the adaptive methods, compared to the ones in uniform grid, especially in shock resolution because of the clustering of grid points near the shock. Again the grid trajectories show the formation and following of the shock layer.

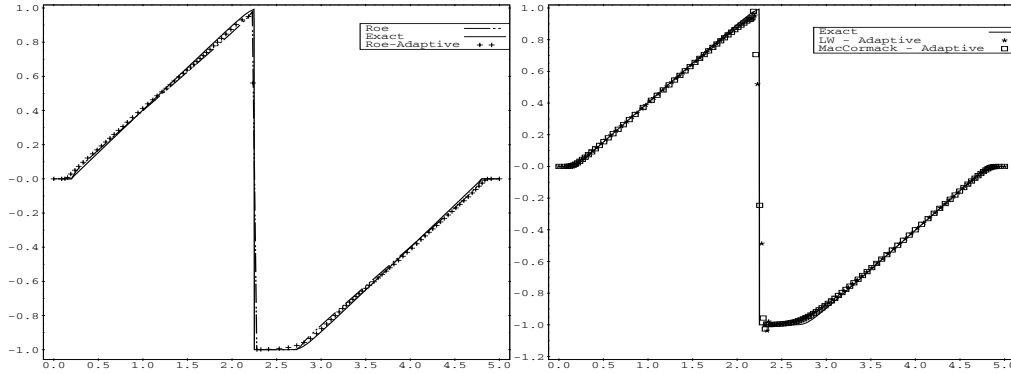


FIG. 5. The second Burgers problem: Numerical solution Roe's scheme (left) ($p = 0.079$, $D = 0.0224$) and the LW and MacCormack schemes (right) ($p = 0.10$, $D = 0$).

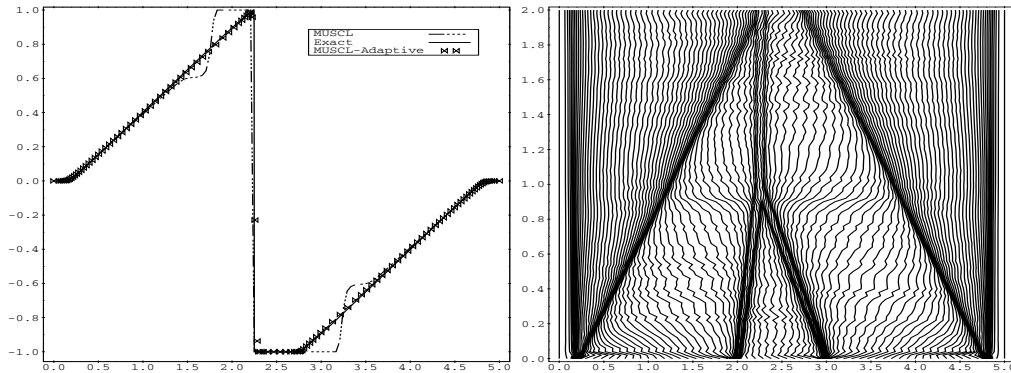


FIG. 6. The second Burgers problem: Numerical solution (left) and grid point trajectories (right) for the adaptive MUSCL scheme ($p = 0.09$, $D = 0$).

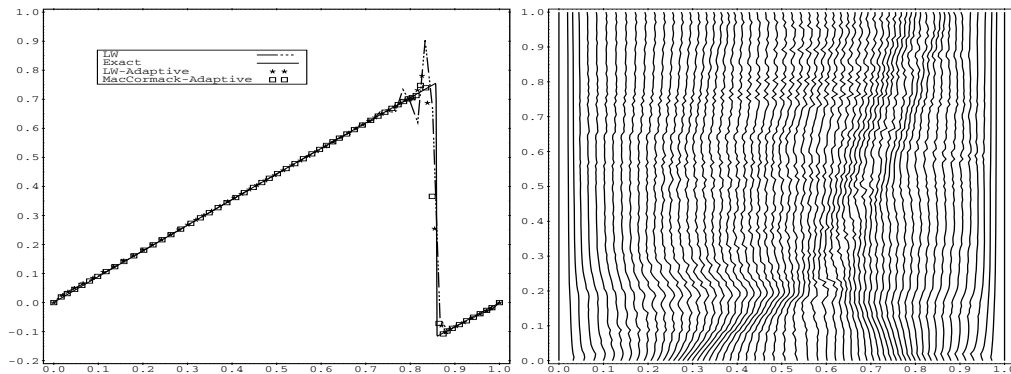


FIG. 7. The third Burgers problem: Numerical solution for the LW and MacCormack schemes (left) and grid point trajectories (right) for the LW scheme ($p = 0.06$, $D = 0$).

The fourth problem has initial condition

$$u(x, 0) = 1 - 0.02x, \quad x \in [0, 100],$$

and has been selected to illustrate convergence to a discontinuous steady state. The

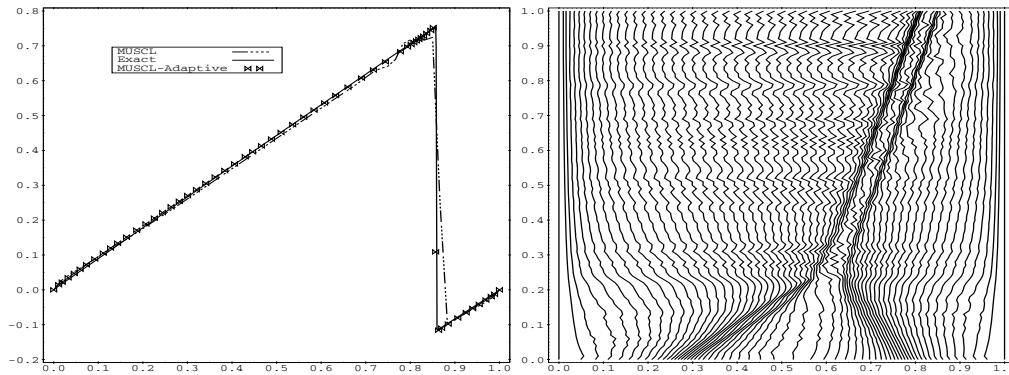


FIG. 8. The third Burgers problem: Numerical solution (left) and grid point trajectories (right) for the MUSCL scheme ($p = 0.118$, $D = 0$).

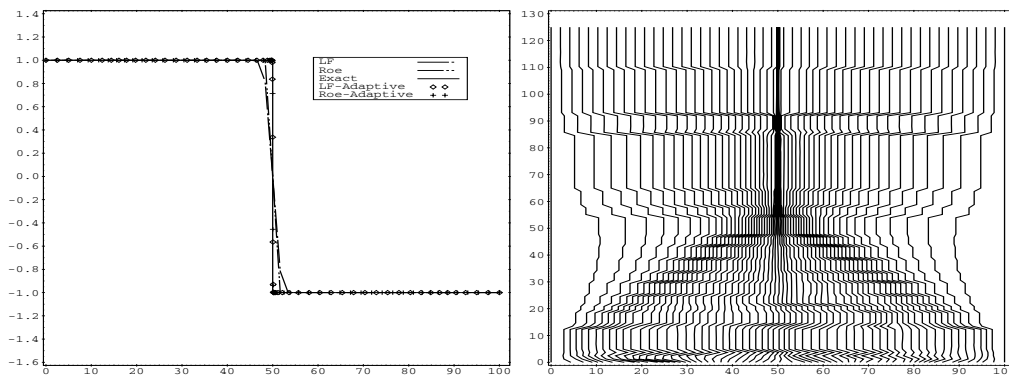


FIG. 9. The fourth Burgers problem: Numerical solutions for the Roe and LF schemes (left) and grid point trajectories (right) for the adaptive Roe scheme ($p = 0.10$, $D = 0.013$).

parameters for the calculations were 61 grid points and a CFL number equal to 0.9. The stabilizing tendency of the adaptive method can be clearly seen since it does not produce oscillatory results, as shown in Figures 9 and 10 for $t = 125s$. One can also observe the improvement in all the calculations when the adaptive mechanism is imposed. The effect in the grid movement of a zero and a nonzero value for the “cutoff” parameter D , for Roe’s first order scheme, can be seen in Figure 11, following the remarks made in section 2.3.

4.2. Nonconvex conservation law and the Buckley–Leverett equation.

In this section we first apply the adaptive grid method to the scalar conservation law with nonlinear nonconvex flux,

$$(4.6) \quad f(u) = (u^2 - 1)(u^2 - 4)/4 \quad \text{for } x \in [0, 1].$$

The initial profile is $u(x, 0) = -2\text{sign}(x)$. As pointed out in [29] solving this Riemann problem for a scalar conservation law with nonconvex flux leads to difficulties with some numerical schemes. Numerical solutions for all schemes are shown in Figure 12 at $t = 1.2s$, in a 101-point grid and for CFL number equal to 0.8. Again by imposing the adaptive mechanism we are able to produce quality results for all schemes.

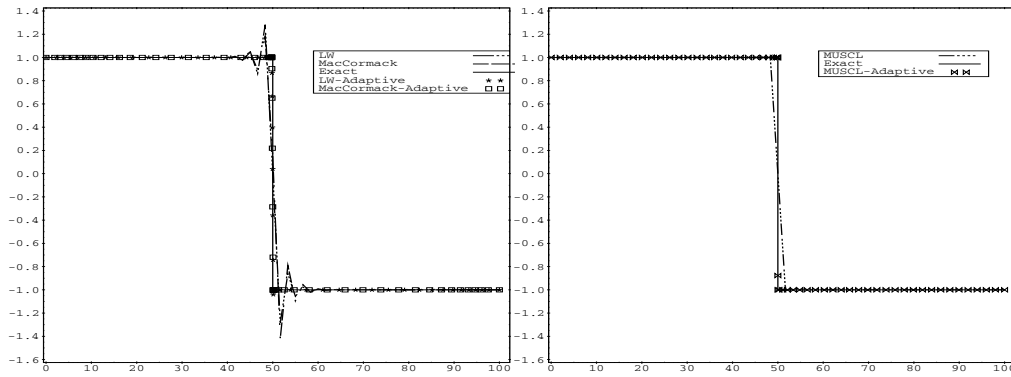


FIG. 10. The fourth Burgers problem: Numerical solutions for the LW and MacCormack schemes (left) and MUSCL scheme (right) ($p = 0.13$, $D = 0$).

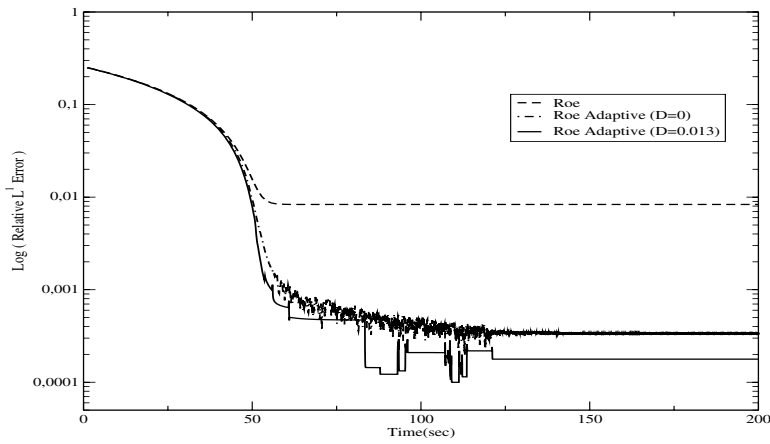


FIG. 11. The fourth Burgers problem: convergence histories for the Roe scheme.

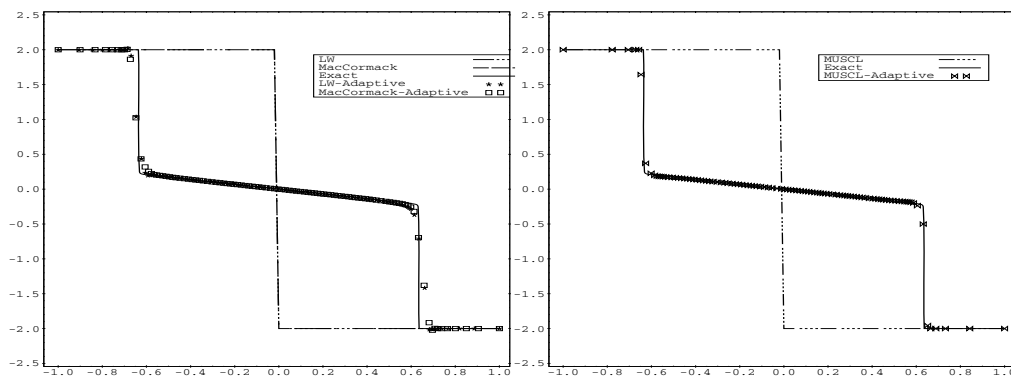


FIG. 12. Nonconvex flux problem: Numerical solutions for the LW and MacCormack schemes (left) and MUSCL scheme (right) ($p = 0.069$, $D = 0$).

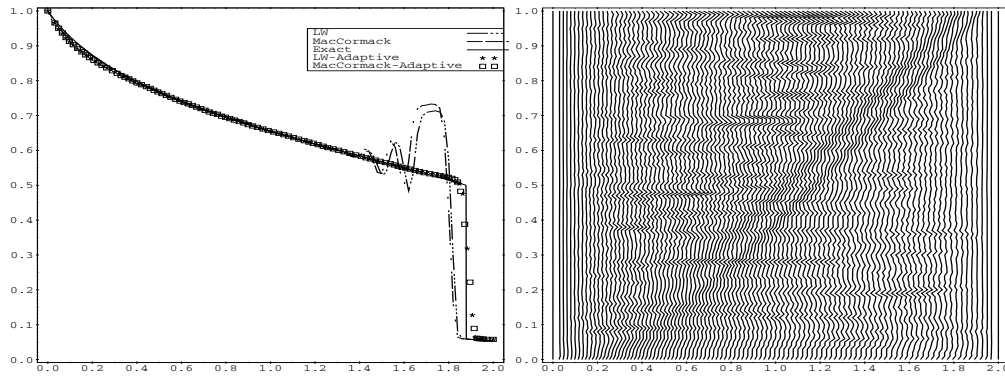


FIG. 13. Buckley-Leverett problem: Numerical solutions for the LW and MacCormack schemes (left) and grid point trajectories for the adaptive LW scheme ($p = 0.076$, $D = 0$).

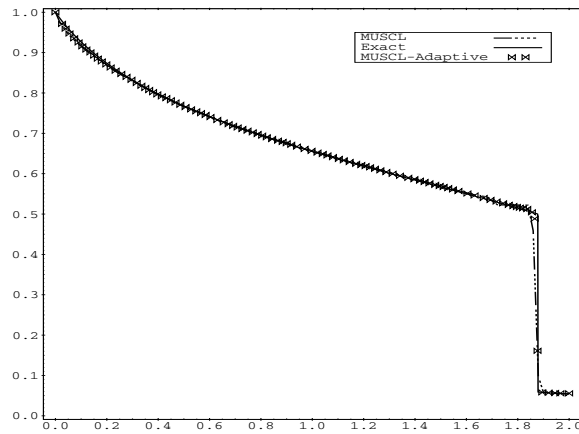


FIG. 14. Buckley-Leverett problem: Numerical solutions for the MUSCL scheme ($p = 0.10$, $D = 0.0088$).

Next we consider the scalar Buckley-Leverett equation with the flux function

$$f(u) = \frac{u^2}{u^2 + 0.5(1 - u)^2},$$

with initial and boundary conditions for $x \in [0, 2]$,

$$u(x, 0) = \frac{1}{1 + 10x}, \quad u(0, t) = 1, \quad u(1, t) = \frac{1}{21}.$$

The solution for the adaptive and uniform LW and MacCormack schemes is shown in Figure 13 in a 101-point grid. The highly oscillatory behavior of these schemes is totally suppressed by the adaptive mechanism resolving and following the shock layer much more accurately. Improvement in the shock resolution can also be observed for the MUSCL scheme in Figure 14.

Remark 4 (a result on the smoothing effect of the AGR). As a final result for scalar CL we present a simple advection test (see [26]) of a contact discontinuity in order to measure the smoothing effect of the adaptive mechanism. We compute an

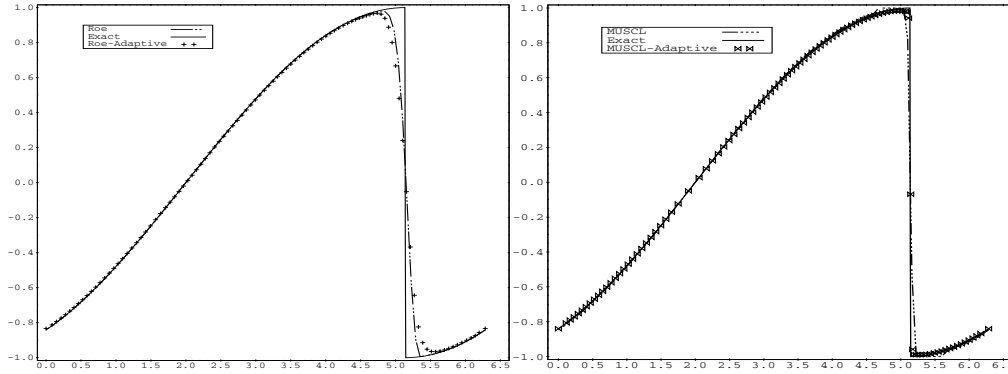


FIG. 15. Linear advection of a contact discontinuity for the Roe scheme ($p = 0.03, D = 0.004$) and MUSCL scheme ($p = 0.12, D = 0$).

approximate solution to the linear advection equation, $u_t + u_x = 0$, with periodic boundary conditions and initial condition

$$u(x, 0) = \begin{cases} \sin(x/2), & x \in [0, \pi), \\ -\sin(x/2), & x \in [\pi, 2\pi), \end{cases}$$

that has a discontinuity at $x = \pi$ which at $t = 2s$ is advected to $x = \pi + 2$. Results on a 101-point grid for the Roe and MUSCL schemes, with $CFL = 0.95$, are shown in Figure 15. The smoothing effect of the adaptive mechanism can be seen for the first order Roe scheme, but for the second order MUSCL scheme the results have been improved.

5. Numerical schemes for nonuniform grids (one-dimensional systems of equations). We consider the general system of conservation laws with a source term added, i.e.,

$$(5.1) \quad \mathbf{U}_t + \mathbf{F}(\mathbf{U})_x = \mathbf{G}(\mathbf{U}), \quad \mathbf{U} \in \mathbb{R}^M;$$

here $\mathbf{F}(\mathbf{U})$ is the flux function and \mathbf{G} is the source term. We can numerically approximate system (5.1) by using the explicit conservative numerical scheme with a source term approximation within the finite difference-volume frame, as

$$(5.2) \quad \mathbf{U}_i^{n+1} = \mathbf{U}_i^n - \frac{\Delta t}{\Delta x_i} [\mathbf{F}_{i+\frac{1}{2}}^n - \mathbf{F}_{i-\frac{1}{2}}^n] + \frac{\Delta t}{\Delta x_i} \tilde{\mathbf{G}}_i^n,$$

where again $\mathbf{F}_{i+\frac{1}{2}}^n, i = 1, 2, \dots, N - 1$, is the numerical flux function, and the approximation of the source term $\tilde{\mathbf{G}}_i^n$ is considered as the cell average value (numerical source integral over the computational cell) satisfying the relationship

$$(5.3) \quad \tilde{\mathbf{G}}_i^n = \frac{1}{\Delta x_i} \int_{x_{i-\frac{1}{2}}}^{x_{i+\frac{1}{2}}} \mathbf{G}(x, \mathbf{U}^n) dx,$$

and after choosing the numerical flux function it remains to choose an appropriate approximation (depending on the scheme used) for the numerical source integral $\tilde{\mathbf{G}}_i^n$.

For the stationary case, $\mathbf{U}_t = 0$, the flux function and source term balance:

$$\mathbf{F}(\mathbf{U})_x = \mathbf{G}(\mathbf{U}).$$

Therefore, an accurate numerical scheme should also balance the numerical flux with the source term approximation,

$$(5.4) \quad \mathbf{F}_{i+\frac{1}{2}}^n - \mathbf{F}_{i-\frac{1}{2}}^n = \tilde{\mathbf{G}}_i^n.$$

The numerical schemes presented next incorporate the numerical source integral in such a way that (5.4) is satisfied.

5.1. Roe’s scheme for systems of conservation laws with source terms.

The numerical flux for the Roe upwind scheme can be written in the form

$$(5.5) \quad \mathbf{F}_{i+\frac{1}{2}}^{\text{ROE}} = \frac{1}{2} \left[\mathbf{F}_{i+1} + \mathbf{F}_i - \mathbf{J}_{i+\frac{1}{2}} (\mathbf{U}_{i+1} - \mathbf{U}_i) \right].$$

The matrix $\mathbf{J}_{i+\frac{1}{2}}$ is the Roe-type linearization and satisfies

$$(5.6) \quad \mathbf{F}_{i+1} - \mathbf{F}_i = \mathbf{J}_{i+\frac{1}{2}} (\mathbf{U}_{i+1} - \mathbf{U}_i)$$

and has real eigenvalues $(\tilde{\alpha}_{i+\frac{1}{2}}^k)$, $k = 1, \dots, M$, and a complete set of eigenvectors $(\tilde{\mathbf{e}}_{i+\frac{1}{2}}^k)$. Representing now $\mathbf{U}_{i+1} - \mathbf{U}_i$ in terms of the eigenvectors of the Roe linearization, i.e.,

$$(5.7) \quad \mathbf{U}_{i+1} - \mathbf{U}_i = \sum_{k=1}^M \alpha_{i+\frac{1}{2}}^k \tilde{\mathbf{e}}_{i+\frac{1}{2}}^k,$$

we obtain from (5.6)

$$(5.8) \quad \mathbf{J}_{i+\frac{1}{2}} (\mathbf{U}_{i+1} - \mathbf{U}_i) = \sum_{k=1}^M \tilde{\alpha}_{i+\frac{1}{2}}^k \alpha_{i+\frac{1}{2}}^k \tilde{\mathbf{e}}_{i+\frac{1}{2}}^k.$$

Then the Roe numerical flux can be written as

$$(5.9) \quad \mathbf{F}_{i+\frac{1}{2}}^{\text{ROE}} = \frac{1}{2} \left[\mathbf{F}_{i+1} + \mathbf{F}_i - \sum_{k=1}^M |\tilde{\alpha}_{i+\frac{1}{2}}^k| \alpha_{i+\frac{1}{2}}^k \tilde{\mathbf{e}}_{i+\frac{1}{2}}^k \right].$$

The $\alpha_{i+\frac{1}{2}}$ (wave strengths) values follow from (5.7).

Source term upwinding. The integral of \mathbf{G} , in relation (5.3), over the cell $[x_{i-\frac{1}{2}}, x_{i+\frac{1}{2}}]$ is first split into a sum of two integrals in the $[x_{i-\frac{1}{2}}, x_i]$, $[x_i, x_{i+\frac{1}{2}}]$ as

$$(5.10) \quad \frac{1}{\Delta x_i} \int_{x_{i-\frac{1}{2}}}^{x_{i+\frac{1}{2}}} \mathbf{G}(x, \mathbf{U}^n) dx = \frac{1}{\Delta x_i} \left[\int_{x_{i-\frac{1}{2}}}^{x_i} \mathbf{G}(x, \mathbf{U}^n) dx + \int_{x_i}^{x_{i+\frac{1}{2}}} \mathbf{G}(x, \mathbf{U}^n) dx \right].$$

The upwind definition of the approximated source terms $\tilde{\mathbf{G}}_i^n$ for nonuniform grids is given by

$$(5.11) \quad \tilde{\mathbf{G}}_i^n = \frac{1}{\Delta x_i} \left[\frac{(x_i - x_{i-1})}{2} \tilde{\mathbf{G}}^L(x_{i-1}, x_i, \mathbf{U}_{i-1}^n, \mathbf{U}_i^n) + \frac{(x_{i+1} - x_i)}{2} \tilde{\mathbf{G}}^R(x_i, x_{i+1}, \mathbf{U}_i^n, \mathbf{U}_{i+1}^n) \right],$$

where $\tilde{\mathbf{G}}^L$ and $\tilde{\mathbf{G}}^R$ are continuous functions, giving the averages of $\mathbf{G}(x, \mathbf{U}^n)$ on the subcells $[x_{i-\frac{1}{2}}, x_i]$, $[x_i, x_{i+\frac{1}{2}}]$, respectively. These functions give the upwind values of the source terms and following [7] can be defined as

$$(5.12) \quad \tilde{\mathbf{G}}_{i-\frac{1}{2}}^L = \left[\mathbf{I} + |\mathbf{J}_{i-\frac{1}{2}}| \mathbf{J}_{i-\frac{1}{2}}^{-1} \right] \tilde{\mathbf{G}}_{i-\frac{1}{2}}, \quad \tilde{\mathbf{G}}_{i+\frac{1}{2}}^R = \left[\mathbf{I} - |\mathbf{J}_{i+\frac{1}{2}}| \mathbf{J}_{i+\frac{1}{2}}^{-1} \right] \tilde{\mathbf{G}}_{i+\frac{1}{2}}.$$

The definition of the $\mathbf{J}_{i\pm\frac{1}{2}}$ and $|\mathbf{J}_{i\pm\frac{1}{2}}|$ matrices follow from (5.6) for the Roe linearization and are defined in the appendix. The terms $\tilde{\mathbf{G}}_{i\pm\frac{1}{2}}$ represent approximations of \mathbf{G} at cells $(i-1, i)$ and $(i, i+1)$, respectively.

Alternatively, we rewrite (5.12) in decomposed form,

$$(5.13) \quad \tilde{\mathbf{G}}_{i-\frac{1}{2}}^L = \sum_{k=1}^M \beta_{i-\frac{1}{2}}^k \tilde{\mathbf{e}}_{i-\frac{1}{2}}^k \left(1 + \text{sgn}(\tilde{a}_{i-\frac{1}{2}}^k) \right), \quad \tilde{\mathbf{G}}_{i+\frac{1}{2}}^R = \sum_{k=1}^M \beta_{i+\frac{1}{2}}^k \tilde{\mathbf{e}}_{i+\frac{1}{2}}^k \left(1 - \text{sgn}(\tilde{a}_{i+\frac{1}{2}}^k) \right),$$

with the values of $\beta_{i\pm\frac{1}{2}}^k$ determined from

$$(5.14) \quad \sum_{k=1}^M \beta_{i\pm\frac{1}{2}}^k \tilde{\mathbf{e}}_{i\pm\frac{1}{2}}^k = \tilde{\mathbf{G}}_{i\pm\frac{1}{2}}.$$

5.2. The LW scheme. The numerical flux for the classical second order LW scheme for nonlinear systems, on nonuniform grids, can be written, following [18], as

$$(5.15) \quad \mathbf{F}_{i+\frac{1}{2}}^{\text{LW}} = \mathbf{F}_{i+\frac{1}{2}}^{\text{ROE}} + \frac{1}{2} \sum_{k=1}^M \left(\frac{\Delta x_i}{\Delta x_{i+\frac{1}{2}}} - \frac{\Delta t}{\Delta x_{i+\frac{1}{2}}} |\tilde{a}_{i+\frac{1}{2}}^k| \right) |\tilde{a}_{i+\frac{1}{2}}^k| \alpha_{i+\frac{1}{2}}^k \tilde{\mathbf{e}}_{i+\frac{1}{2}}^k,$$

where $\Delta x_{i+\frac{1}{2}} = (\Delta x_{i+1} + \Delta x_i)/2$.

A flux-limited second order TVD version of the LW scheme is then given by

$$(5.16) \quad \mathbf{F}_{i+\frac{1}{2}}^{\text{LWTV}} = \mathbf{F}_{i+\frac{1}{2}}^{\text{ROE}} + \frac{1}{2} \sum_{k=1}^M \left(\frac{\Delta x_i}{\Delta x_{i+\frac{1}{2}}} - \frac{\Delta t}{\Delta x_{i+\frac{1}{2}}} |\tilde{a}_{i+\frac{1}{2}}^k| \right) \Phi(\theta_{i+\frac{1}{2}}^k) |\tilde{a}_{i+\frac{1}{2}}^k| \alpha_{i+\frac{1}{2}}^k \tilde{\mathbf{e}}_{i+\frac{1}{2}}^k,$$

where

$$(5.17) \quad \theta_{i+\frac{1}{2}}^k = \frac{\alpha_{I+\frac{1}{2}}^k}{\alpha_{i+\frac{1}{2}}^k} \quad \text{with} \quad I = \begin{cases} i-1 & \text{if } \tilde{a}_{i+\frac{1}{2}}^k > 0, \\ i+1 & \text{if } \tilde{a}_{i+\frac{1}{2}}^k < 0; \end{cases}$$

here Φ can be any of the limiter functions presented in section 3.

The Roe averaged values can be used for the source term approximations, and we obtain a flux-limited second order approximation of the source term in the numerical source term (5.10), similar to the one presented in [16], by setting

$$\tilde{\mathbf{G}}_{i-\frac{1}{2}}^L = \sum_{k=1}^M \beta_{i-\frac{1}{2}}^k \tilde{\mathbf{e}}_{i-\frac{1}{2}}^k \left[1 + \text{sgn}(\tilde{a}_{i-\frac{1}{2}}^k) \left(1 - \Phi(\theta_{i-\frac{1}{2}}^k) \left(\frac{\Delta x_i}{\Delta x_{i-\frac{1}{2}}} - \frac{\Delta t}{\Delta x_{i-\frac{1}{2}}} |\tilde{a}_{i-\frac{1}{2}}^k| \right) \right) \right],$$

$$\tilde{\mathbf{G}}_{i+\frac{1}{2}}^R = \sum_{k=1}^M \beta_{i+\frac{1}{2}}^k \tilde{\mathbf{e}}_{i+\frac{1}{2}}^k \left[1 - \text{sgn}(\tilde{a}_{i+\frac{1}{2}}^k) \left(1 - \Phi(\theta_{i+\frac{1}{2}}^k) \left(\frac{\Delta x_i}{\Delta x_{i+\frac{1}{2}}} - \frac{\Delta t}{\Delta x_{i+\frac{1}{2}}} |\tilde{a}_{i+\frac{1}{2}}^k| \right) \right) \right].$$

5.3. The MacCormack scheme. The MacCormack scheme adapted to approximate systems of conservation laws with a source term can be written as

$$(5.18) \quad \mathbf{U}_i^{n+1} = \frac{1}{2} \left(\mathbf{U}_i^n + \mathbf{U}_i^{(1)} \right) - \frac{\Delta t}{2\Delta x_i} \left(\mathbf{F}_i^{(1)} - \mathbf{F}_{i-1}^{(1)} \right) + \frac{\Delta t}{2\Delta x_i} \tilde{\mathbf{G}}_{i-\frac{1}{2}}^{(1)},$$

where

$$\mathbf{U}_i^{(1)} = \mathbf{U}_i^n - \frac{\Delta t}{\Delta x_i} \left(\mathbf{F}_{i+1}^n - \mathbf{F}_i^n \right) + \frac{\Delta t}{\Delta x_i} \tilde{\mathbf{G}}_{i+\frac{1}{2}}^n.$$

This scheme is a predictor-corrector one and has the advantage that we do not need to approximate the eigenvalues and eigenvectors of the Jacobian matrix. However, spurious oscillations may occur in the solution, especially when discontinuities are present, even when we choose the $\tilde{\mathbf{G}}$ discretizations in (5.18) in such a way as to satisfy (5.4).

6. The shallow water model. We consider the well-known one-dimensional shallow water system, with a geometrical source term (the bottom topography) added, written in differential conservation law form as a single vector equation:

$$(6.1) \quad \mathbf{U}_t + \mathbf{F}(\mathbf{U})_x = \mathbf{G}(\mathbf{U}),$$

with

$$\mathbf{U} = \begin{bmatrix} h \\ hu \end{bmatrix}, \quad \mathbf{F}(\mathbf{U}) = \begin{bmatrix} hu \\ hu^2 + \frac{g}{2}h^2 \end{bmatrix}, \quad \mathbf{G}(\mathbf{U}) = \begin{bmatrix} 0 \\ -ghZ' \end{bmatrix}.$$

System (6.1) describes the flow at time $t \geq 0$ at point $x \in \mathbb{R}$, where $h(x, t) \geq 0$ is the total water height above the bottom, $u(x, t)$ is the average horizontal velocity, $Z(x)$ is the bottom height function, and g the gravitational acceleration. In the following we will denote by $q = hu$ the water unit discharge.

An important property of system (6.1) is related to the source term: the shallow water system admits nontrivial steady states. They are characterized by

$$(6.2) \quad (hu)_x = 0,$$

$$(6.3) \quad \left(hu^2 + \frac{g}{2}h^2 \right)_x = ghZ',$$

i.e.,

$$(6.4) \quad q = (hu) = \text{constant},$$

$$(6.5) \quad hu^2 + g(h + Z) = \text{constant}.$$

A particular case that provides a benchmark for many approximating schemes is the still water steady state (flow at rest), i.e., when $u = 0$ and $h + Z = \text{constant}$.

In [7] the concept of Property C was introduced. A given scheme would satisfy Property C if, in the case of a flow at rest, there is an exact balance between the discrete components of the flux and a given source term treatment based on (5.4), approximating this stationary solution. Thus, when numerically treating the source terms, for Property C to be satisfied exactly or approximately (to order $O(\Delta x^2)$) one must ensure that this equilibrium solution would not be perturbed. The source term discretizations presented in the previous sections along with those presented in the appendix for the shallow water system satisfy this property.

In the numerical examples presented next we use again a variable time step as to satisfy the $\text{CFL} \leq 1$ stability condition:

$$(6.6) \quad \text{CFL} = \Delta t \max_{i,k} \left\{ \left| \frac{\tilde{a}_{i-\frac{1}{2}}^{k+}}{\Delta x_i} \right|, \left| \frac{\tilde{a}_{i+\frac{1}{2}}^{k-}}{\Delta x_i} \right| \right\},$$

where for the shallow water model values $\tilde{a}_{i-\frac{1}{2}}^{k+}$ and $\tilde{a}_{i+\frac{1}{2}}^{k-}$ are defined in the appendix.

6.1. Idealized dam-break flow. We first consider a nonstationary case, the dam-break problem in a rectangular channel with flat bottom, $Z = 0$. We computed the solution on a channel of length $L = 2000\text{m}$ for time $t = 50\text{s}$ and with initial conditions

$$\begin{aligned} u(x, 0) &= 0, \\ h(x, 0) &= \begin{cases} h_1, & x \leq 1000, \\ h_0, & x > 1000, \end{cases} \end{aligned}$$

with $h_1 > h_0$. This is the corresponding Riemann problem for the homogeneous problem. The water depth ratio is given by h_0/h_1 . The dam collapses at $t = 0\text{s}$ and the resulting flow consists of a shock wave (bore) traveling downstream and a rarefaction wave (depression wave) traveling upstream. The upstream depth h_1 was set at 10m . When the depth ratio is greater than 0.5 , the flow throughout the channel remains subcritical. For depth ratios smaller than 0.5 , the flow downstream of the dam position is supercritical while remaining subcritical upstream. For very small values of the ratio h_0/h_1 the flow regime becomes strongly supercritical downstream and the shock wave can be difficult to capture; see [10], for example. Analytical solutions to this problem can be found, for example, in [24].

Comparative results are presented in a 101-point grid and depth ratio 0.005 , for all schemes in Figures 16–18, using $\text{CFL} = 0.9$. All the results produced with the adaptive method are significantly better in terms of shock resolution and nonoscillatory behavior in both components of the solution. No entropy problems appeared for all adaptive schemes. The grid clustering and the close following of the downstream shocks can also be seen. It is impressive that the LW and MacCormack schemes are able to produce quality results with no extra dissipative mechanism imposed other than the adaptive one. The performance of the TVD scheme, using the VL limiter, was also improved.

A more quantitative comparison is afforded in Table 1, where we compare the adaptive and nonadaptive Roe and TVD schemes in terms of computational costs, reported as the CPU times, the number of time steps (NT), and the L^1 errors for h and q . It is clear that the adaptive schemes produce accurate results with fewer grid points than the nonadaptive schemes, and even though the total number of time steps is increased, for the adaptive schemes, CPU times are substantially smaller (since in nonadaptive schemes one has to obtain solutions to many more grid points). For example, the adaptive grid calculations with 101 grid points are as accurate as for a fixed grid with 401 points, and require less CPU time. The effect of the parameter D can also be seen in Table 1.

6.2. Flow at rest over topography. We consider system (6.1) with initial conditions

$$\begin{aligned} u(x, 0) &= 0 \quad \forall x \in \mathbb{R}, \\ h(x, 0) + Z(x) &= H \quad \forall x \in \mathbb{R}. \end{aligned}$$

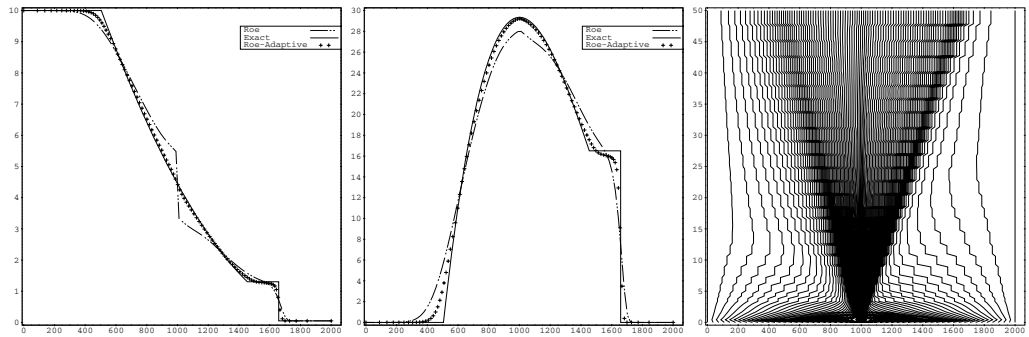


FIG. 16. Idealized dam-break flow: results with Roe's scheme for h (left), q (middle), and grid point trajectories (right) for the adaptive Roe scheme ($p = 0.0518$, $D = 0.0065$).

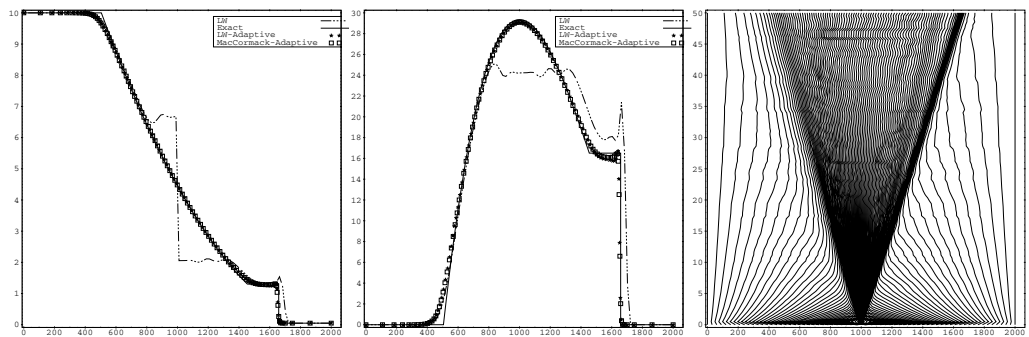


FIG. 17. Idealized dam-break flow: results with the LW and MacCormack schemes for h (left), q (middle), and grid point trajectories (right) for the adaptive LW scheme ($p = 0.10$, $D = 0$).

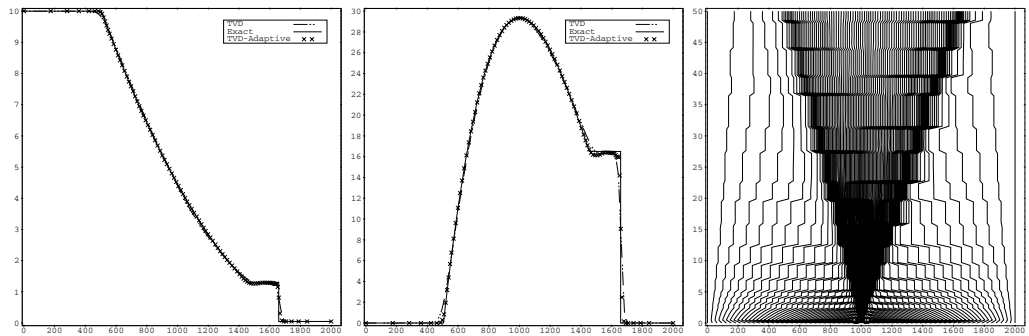


FIG. 18. Idealized dam-break flow: results with the TVD scheme for h (left), q (middle), and grid point trajectories (right) for the adaptive TVD scheme ($p = 0.10$, $D = 0.0125$).

Then, clearly,

$$\begin{aligned} u(x, t) &= 0 \quad \forall x \in \mathbb{R}, t \geq 0, \\ h(x, t) + Z(x) &= H \quad \forall x \in \mathbb{R}, t \geq 0 \end{aligned}$$

is a solution to (6.1).

We test the schemes with the adaptive mechanism in order to study their behavior

TABLE 1
Idealized dam-break flow: comparative performance of the Roe and TVD schemes.

Description	CPU time (sec)	NT	L^1 error (h)	L^1 error (q)
Roe Fixed grid:				
$N = 51$	0.0051	21	0.0170	0.0393
$N = 101$	0.0206	43	0.0113	0.0240
$N = 201$	0.0828	87	0.0077	0.0169
$N = 401$	0.3401	178	0.0049	0.0102
Roe + AGR:				
$N = 51, p = 0.0500, D = 0.0065$	0.0234	77	0.0091	0.0238
$N = 101, p = 0.0350, D = 0$	0.0583	97	0.0080	0.0220
$N = 101, p = 0.0500, D = 0$	0.1072	178	0.0061	0.0176
$N = 101, p = 0.0500, D = 0.0065$	0.0931	158	0.0049	0.0137
TVD Fixed grid:				
$N = 51$	0.0112	22	0.0050	0.0156
$N = 101$	0.0450	44	0.0028	0.0078
$N = 201$	0.1837	90	0.0009	0.0025
$N = 401$	0.7432	180	0.0007	0.0020
TVD + AGR:				
$N = 51, p = 0.1, D = 0.0125$	0.0788	136	0.0029	0.0076
$N = 101, p = 0.1, D = 0$	0.4292	369	0.0018	0.0055
$N = 101, p = 0.1, D = 0.0125$	0.3927	342	0.0007	0.0023

to this benchmark problem [13, 9, 11] with $Z(x)$ given by

$$(6.7) \quad Z(x) = \begin{cases} 0.2 - 0.05(x - 10)^2, & 8 \leq x \leq 12, \\ 0 & \text{otherwise,} \end{cases}$$

in a channel of length $L = 25\text{m}$ and $H = 2\text{m}$. Figures 19 and 20 display the final water level and the final unit discharge values, respectively, for the Roe and MacCormack schemes at time $t = 200\text{s}$ and in a grid of 101 points. Both schemes with the adaptation method perfectly preserve this steady state, up to machine accuracy. Grid points are concentrated where most needed, in the topography area. The movement of the grid points is stopping much faster for the MacCormack scheme being a second order method in time. Similar results and observations were made for the TVD scheme that are not presented here for brevity.

6.3. Steady transcritical flow. In this case, and for the same initial conditions as in section 6.2, we impose an upstream boundary condition for the discharge $q = 1.53\text{m}^2/\text{s}$ and a downstream boundary condition for the water level $H_0 = 0.66\text{m}$ only in the case where the flow is subcritical. If the flow becomes supercritical downstream, no condition for the water level is imposed. Results at $t = 250\text{s}$ in a 51-point grid are presented in Figures 21 and 22 for the Roe and TVD schemes (using the MM limiter) and $\text{CFL} = 0.9$.

In Table 2 we quantify the errors and performance of the schemes for this test problem. Similar observations with those in section 6.1 can be deduced. The importance of using the parameter D for steady state problems can be clearly seen.

6.4. Steady transcritical flow with shock. The initial conditions in this case was taken to be as in the previous section, with H being the constant water level downstream provided by the boundary condition. In this test case the upstream boundary condition for the discharge was $q = 0.18\text{m}^2/\text{s}$ and the downstream boundary condition for the water level was $H = 0.33\text{m}$.

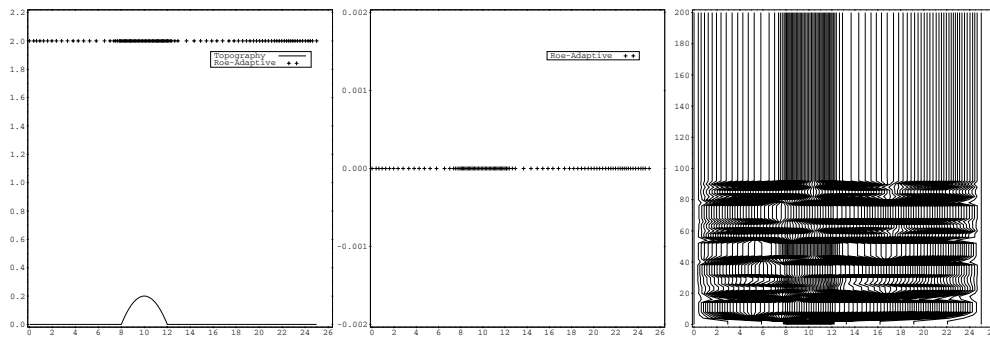


FIG. 19. Flow at rest over topography: results with the adaptive Roe scheme for $h + Z$ (left), q (middle), and grid point trajectories (right) ($p = 0.06$, $D = 0.0525$).

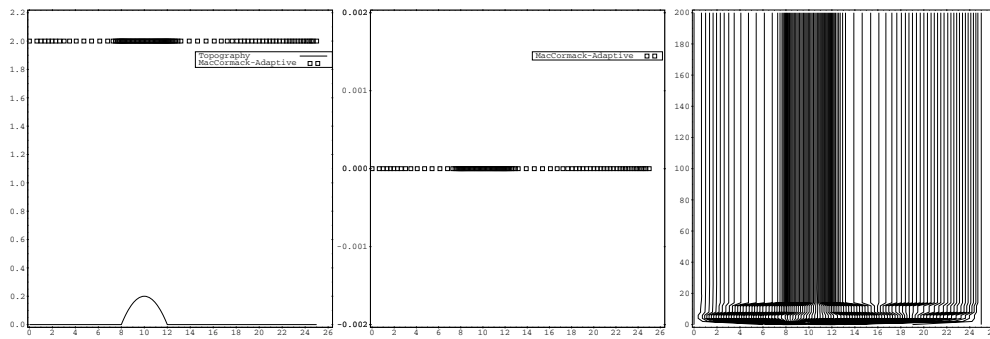


FIG. 20. Flow at rest over topography: results with the adaptive MacCormack scheme for $h + Z$ (left), q (middle), and grid point trajectories (right) ($p = 0.06$, $D = 0.0525$).

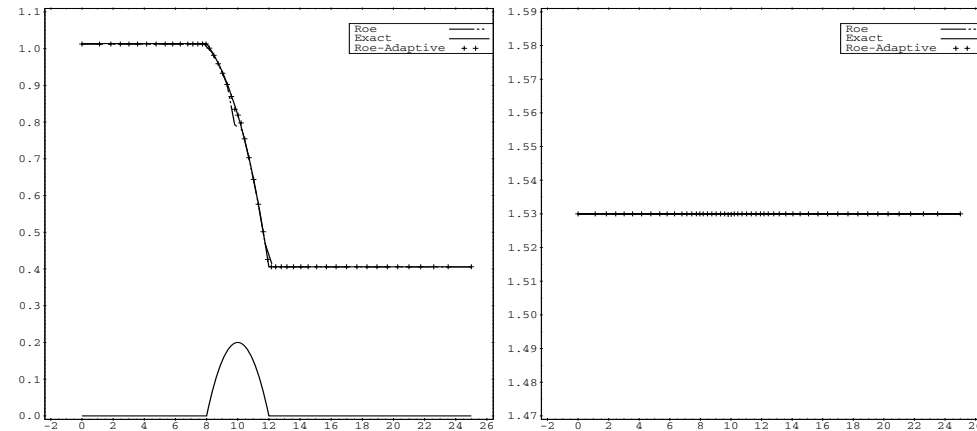


FIG. 21. Steady transcritical flow: results with Roe's scheme for $h + Z$ (left), discharge (q) (right) ($p = 0.075$, $D = 0.06$).

Results for a coarse 51-point grid for the Roe and TVD schemes and also on a 101-point grid for the TVD scheme with the MM limiter used are shown in Figures 23–25. The improvement in the results compared to the uniform grid results is clear. The shock resolution is very good and the steady state is perfectly preserved for a

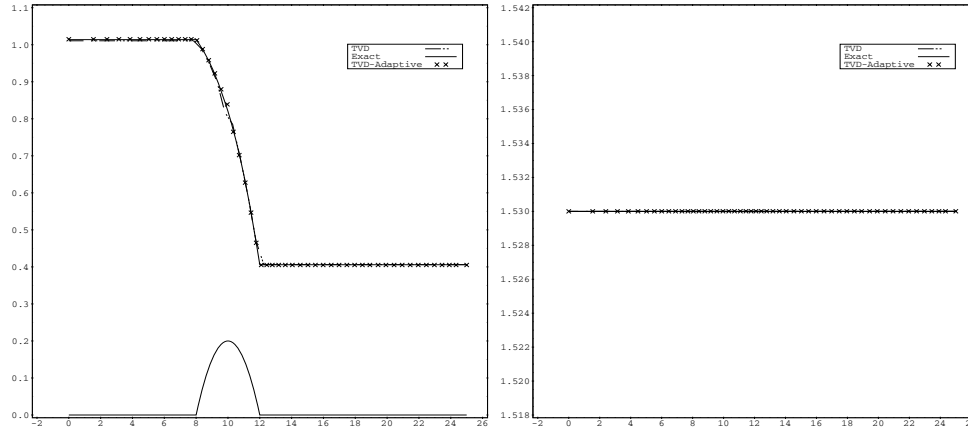


FIG. 22. Steady transcritical flow: results with the TVD scheme for depth $h+Z$ (left), discharge q (right) ($p = 0.1, D = 0.05$).

TABLE 2
Steady transcritical flow: performance of the Roe and TVD schemes.

Description	CPU time (sec)	NT	L^1 error (h)	L^1 error (q)
Roe Fixed grid:				
$N = 101$	3.352	6115	$1.85 \cdot 10^{-3}$	$1.54 \cdot 10^{-5}$
$N = 201$	13.25	12177	$8.81 \cdot 10^{-4}$	$9.63 \cdot 10^{-6}$
$N = 401$	53.51	24304	$2.49 \cdot 10^{-4}$	$5.54 \cdot 10^{-6}$
Roe + AGR:				
$N = 51, p = 0.0750, D = 0.06$	2.150	6504	$1.18 \cdot 10^{-3}$	$9.64 \cdot 10^{-6}$
$N = 101, p = 0.0750, D = 0.06$	9.563	14824	$4.94 \cdot 10^{-4}$	$7.78 \cdot 10^{-6}$
$N = 101, p = 0.0750, D = 0$	9.529	14364	$1.04 \cdot 10^{-2}$	$1.63 \cdot 10^{-3}$
TVD Fixed grid:				
$N = 101$	6.292	6166	$1.27 \cdot 10^{-3}$	$4.83 \cdot 10^{-7}$
$N = 201$	24.84	12273	$3.71 \cdot 10^{-4}$	$3.24 \cdot 10^{-7}$
TVD + AGR:				
$N = 51, p = 0.1, D = 0.05$	3.350	5975	$6.04 \cdot 10^{-4}$	$2.60 \cdot 10^{-7}$
$N = 101, p = 0.1, D = 0.05$	23.17	20747	$4.56 \cdot 10^{-4}$	$2.53 \cdot 10^{-7}$
$N = 101, p = 0.1, D = 0$	21.31	18693	$9.16 \cdot 10^{-3}$	$1.54 \cdot 10^{-3}$

long time calculation of $t = 800s$. The CFL value used in all tests was 0.8.

Finally in Figure 26 the numerical results for the depth are shown for the adaptive MacCormack scheme, where in spite of the formation of a strong shock the scheme can produce a nonoscillatory steady state solution, especially when applying the parameter D .

6.5. Dam-break flow over topography. In this example we solve the shallow water equations with a wavy bottom $Z(x)$,

$$(6.8) \quad Z(x) = \begin{cases} 0.3(\cos(\pi(x-1)/2))^{30}, & |x-1| \leq 1, \\ 0 & \text{otherwise,} \end{cases}$$

and initial conditions

$$(6.9) \quad h(x, 0) = \begin{cases} 2.0 - Z(x), & -10 \leq x < 1, \\ .35 - Z(x), & 1 \leq x < 10, \end{cases} \quad u(x, 0) = \begin{cases} 1, & -10 \leq x < 1, \\ 0, & 1 \leq x < 10, \end{cases}$$

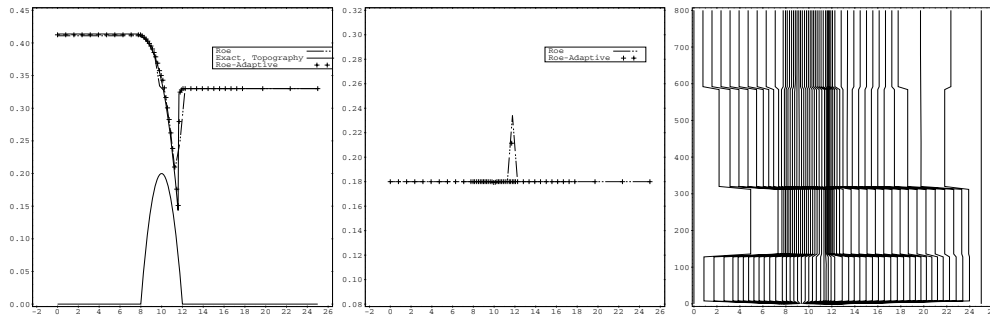


FIG. 23. Steady transcritical flow with shock: results with Roe's scheme for $h + Z$ (left), q (middle), and grid point trajectories (right) for the adaptive Roe scheme ($p = 0.08$, $D = 0.07$).

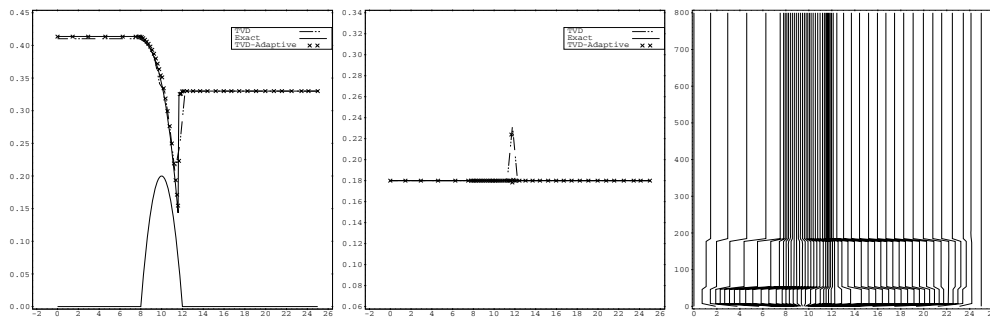


FIG. 24. Steady transcritical flow with shock: results with the TVD scheme for $h + Z$ (left), q (middle), and grid point trajectories (right) for the adaptive TVD scheme on a 51-point grid ($p = 0.08$, $D = 0.075$).

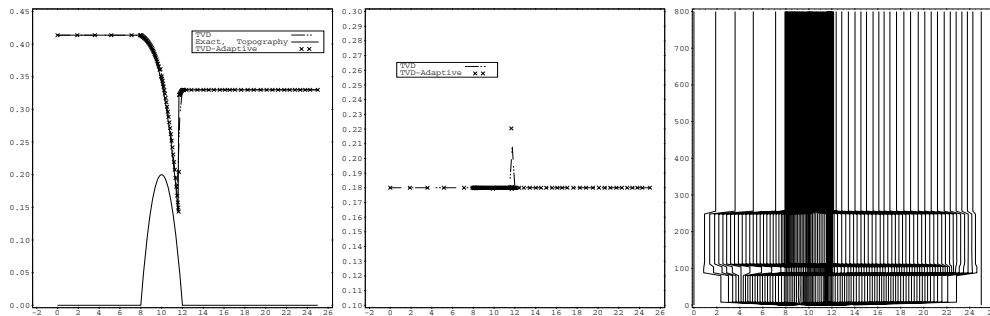


FIG. 25. Steady transcritical flow with shock: results with the TVD scheme for $h + Z$ (left), q (middle), and grid point trajectories (right) for the adaptive TVD scheme on a 101-point grid ($p = 0.08$, $D = 0.075$).

in order to test the adaptive behavior of the schemes in an unsteady flow over topography; this test was also presented in [28]. The solution profiles for the water depth and velocity profile at time $t = 1$ s are shown in Figures 27–29. A grid of 101 points was used in all calculations. The exact solution for this problem is a reference solution calculated in a uniform grid with 4001 grid points. The improvements in the numerical solution can be observed for all the schemes; even the MacCormack scheme can produce a stable solution when compared with the one calculated in a uniform grid.

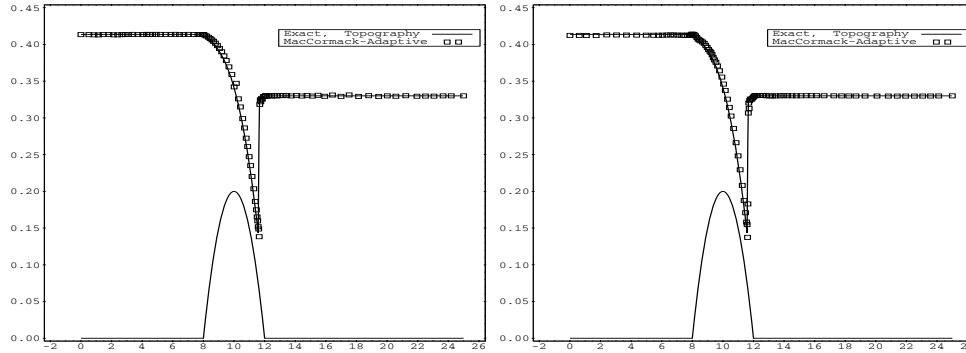


FIG. 26. Steady transcritical flow with shock: results for $h + Z$ with the adaptive MacCormack scheme with $p = 0.12$, $D = 0$ (left) and with $p = 0.12$, $D = 0.003$ (right).

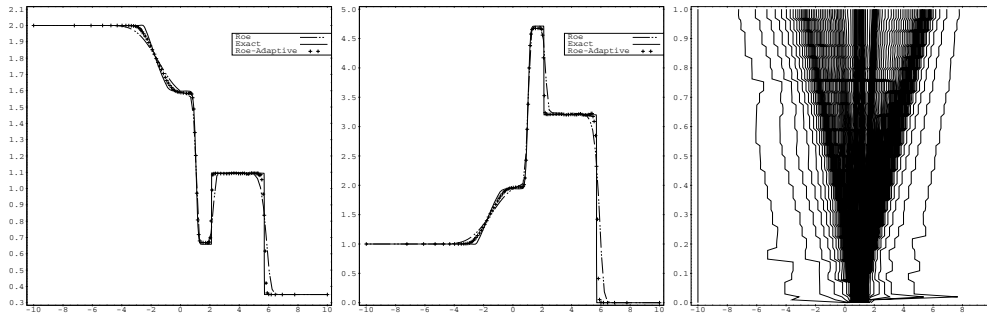


FIG. 27. Dam-break flow over topography: results with Roe's scheme for h (left), u (middle), and grid point trajectories (right) for the adaptive Roe scheme ($p = 0.109$, $D = 0.005$).

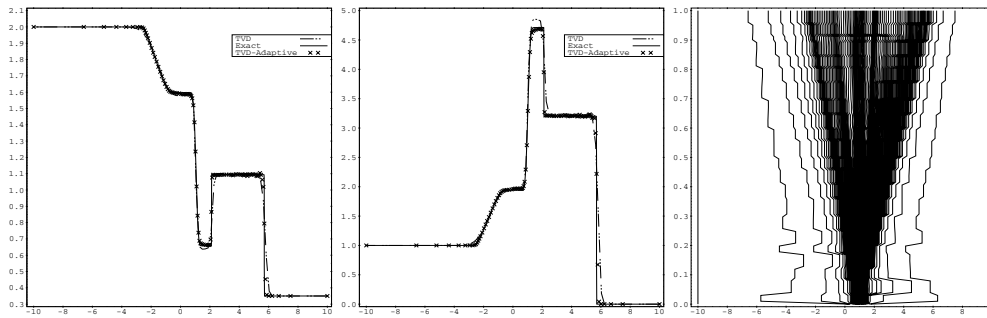


FIG. 28. Dam-break flow over topography: results with the TVD scheme for h (left), u (middle), and grid point trajectories (right) for the adaptive TVD scheme ($p = 0.11$, $D = 0.006$).

7. Conclusions. In this work we have rigorously investigated, in a general framework, the numerical behavior of an adaptive grid redistribution (AGR) mechanism, when combined with classical finite volume numerical methods with well-known characteristics, for solving one-dimensional hyperbolic conservation laws. The evolving mesh is constructed such that its spatial resolution is controlled via selective geometrical characteristics of the numerical solution, by choosing some power of the curvature of the solution as the estimator function. A conservative reconstruction procedure for the numerical solution is also applied at each evolution step.

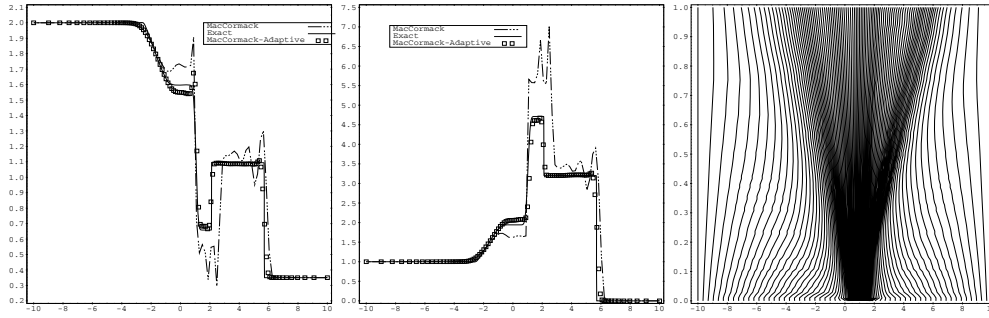


FIG. 29. Dam-break flow over topography: results with the MacCormack scheme for h (left), u (middle), and grid point trajectories (right) for the adaptive MacCormack scheme ($p = 0.0345$, $D = 0.001$).

From the numerical experiments produced in the course of this work we concluded the following advantages of the use of this particular AGR method. The method, when applied to classical second order schemes that compute oscillatory solutions, suppresses the oscillations produced, and as such, classical schemes like the Lax–Wendroff or the MacCormack scheme become stable and can produce reliable solutions. When applied to numerical schemes that do not satisfy entropy conditions, the mechanism can converge to the entropy satisfying solution. The method performs well with hyperbolic problems with source terms by producing stable solutions for first and second order balanced schemes that converge to the correct steady states. The method can automatically detect, resolve, and track steep wave fronts and discontinuities, without having to resort to finer grids. It can be combined with a high resolution flux or slope-limiting TVD scheme and improve the numerical solutions obtained. Only two computational parameters have to be tuned for each problem: the power of the estimator function and the tolerance that measures the relative mean displacement between two consecutive grid distributions, under which the reconstruction step is avoided. The mechanism has been proved robust for all applications presented and schemes used.

There is a need for further theoretical work and development of the method, as well as extension of the ideas presented in this work to higher dimensions. These will provide a more in-depth understanding of the method’s behavior, the advantages gained when the adaptive mechanism is combined with existing numerical schemes, and, more generally, the influence of evolving adaptive grids to the numerical solution of evolution PDEs.

Appendix. Following [7] and [9] the average velocity and celerity, $\tilde{u}_{i+\frac{1}{2}}$ and $\tilde{c}_{i+\frac{1}{2}}$, for the eigenvalues $\tilde{a}_{i+\frac{1}{2}}^{1,2} = \tilde{u}_{i+\frac{1}{2}} \pm \tilde{c}_{i+\frac{1}{2}}$ and eigenvectors, and $\tilde{\mathbf{e}}_{i+\frac{1}{2}}^{1,2} = (1, \tilde{a}_{i+\frac{1}{2}}^{1,2})^T$ of Roe’s linearized Jacobian $\mathbf{J}_{i+\frac{1}{2}}$ for the shallow water system, are calculated as

$$(A.1) \quad \tilde{u}_{i+\frac{1}{2}} = \frac{u_{i+1}\sqrt{h_{i+1}} + u_i\sqrt{h_i}}{\sqrt{h_{i+1}} + \sqrt{h_i}}, \quad \tilde{c}_{i+\frac{1}{2}} = \sqrt{g\tilde{h}},$$

with $\tilde{h} = (h_{i+1} + h_i)/2$.

The wave strengths $\alpha_{i+\frac{1}{2}}^{1,2}$ follow solving (5.7), and they are

$$(A.2) \quad \alpha_{i+\frac{1}{2}}^{1,2} = \frac{1}{2}\Delta_{i+\frac{1}{2}}h \pm \frac{1}{2\tilde{c}_{i+\frac{1}{2}}}(\Delta_{i+\frac{1}{2}}(uh) - \tilde{u}_{i+\frac{1}{2}}\Delta_{i+\frac{1}{2}}h),$$

where the operator $\Delta_{i+\frac{1}{2}}(\cdot) = (\cdot)_{i+1} - (\cdot)_i$.

For a general system of equations and temporarily dropping the subscript indices we define $\mathbf{\Lambda}$ to be the diagonal form of \mathbf{J} given by its eigenvalues, with

$$(A.3) \quad \mathbf{J} = \mathbf{R}\mathbf{\Lambda}\mathbf{R}^{-1},$$

where \mathbf{R} is the matrix of the eigenvectors of \mathbf{J} . We can now define the $|\mathbf{\Lambda}|$, $\mathbf{\Lambda}^+$, and $\mathbf{\Lambda}^-$ matrices as

$$(A.4) \quad |\mathbf{\Lambda}| = \text{diag}(|a^1|, \dots, |a^M|), \quad \mathbf{\Lambda}^\pm = \text{diag}(a^{1^\pm}, \dots, a^{M^\pm}),$$

where $a^{k^+} = \max(0, a^k)$ and $a^{k^-} = \min(0, a^k)$. We can now define

$$(A.5) \quad |\mathbf{J}| = \mathbf{R}|\mathbf{\Lambda}|\mathbf{R}^{-1},$$

$$(A.6) \quad \mathbf{J}^\pm = \mathbf{R}\mathbf{\Lambda}^\pm\mathbf{R}^{-1}.$$

Therefore,

$$(A.7) \quad |\mathbf{J}| = \mathbf{J}^+ - \mathbf{J}^-, \quad \mathbf{J}^\pm = \frac{1}{2}(\mathbf{J} \pm |\mathbf{J}|).$$

Now at the discrete level the $\mathbf{J}_{i+\frac{1}{2}}$ and $|\mathbf{J}_{i+\frac{1}{2}}|$ are defined as

$$(A.8) \quad \mathbf{J}_{i+\frac{1}{2}} = \mathbf{R}_{i+\frac{1}{2}}\mathbf{\Lambda}_{i+\frac{1}{2}}\mathbf{R}_{i+\frac{1}{2}}^{-1},$$

$$(A.9) \quad |\mathbf{J}_{i+\frac{1}{2}}| = \mathbf{R}_{i+\frac{1}{2}}|\mathbf{\Lambda}_{i+\frac{1}{2}}|\mathbf{R}_{i+\frac{1}{2}}^{-1}.$$

Using the above formulation to calculate the upwind approximation of the source term \mathbf{G} , we need to evaluate $\tilde{\mathbf{G}}_{i\pm\frac{1}{2}}$ approximations, that is, some average of the source term on the left and right of the cell interfaces. Then a well-balanced approximation of the source term, at each computational cell, is

$$(A.10) \quad \tilde{\mathbf{G}}_{i\pm\frac{1}{2}} = \left[0, -\frac{g}{2}(h_{i+1} + h_i)(Z_{i+1} - Z_i) \right]^T.$$

The values of $\beta_{i\pm\frac{1}{2}}^{1,2}$ in (5.14) are the components of $\mathbf{R}_{i+\frac{1}{2}}^{-1}\tilde{\mathbf{G}}_{i\pm\frac{1}{2}}$, and for the shallow water system they are

$$\beta_{i\pm\frac{1}{2}}^{1,2} = \mp \frac{\tilde{c}_{i+\frac{1}{2}}(Z_{i+1} - Z_i)}{2}.$$

Acknowledgment. The authors wish to thank Prof. Ch. Makridakis for his helpful discussions during the course of this work.

REFERENCES

- [1] CH. ARVANITIS, TH. KATSAOUNIS, AND CH. MAKRIDAKIS, *Adaptive finite element relaxation schemes for hyperbolic conservation laws*, M2AN Math. Model. Numer. Anal., 35 (2001), pp. 17–33.
- [2] CH. ARVANITIS, CH. MAKRIDAKIS, AND A. E. TZAVARAS, *Stability and convergence of a class of finite element schemes for hyperbolic systems of conservation laws*, SIAM J. Numer. Anal., 42 (2004), pp. 1357–1393.

- [3] CH. ARVANITIS, *Mesh redistribution strategies and finite element schemes for hyperbolic conservation laws*, submitted.
- [4] B. N. AZARENOK AND T. TANG, *Second-order Godunov-type scheme for reactive flow calculations on moving meshes*, J. Comput. Phys., 206 (2005), pp. 48–80.
- [5] B. N. AZARENOK, S. A. IVANENKO, AND T. TANG, *Adaptive mesh redistribution method based on Godunov's scheme*, Commun. Math. Sci., 1 (2003), pp. 152–179.
- [6] G. BECKETT AND J. A. MACKENZIE, *Convergence analysis of finite difference approximations on equidistributed grids to a singularly perturbed boundary value problem*, Appl. Numer. Math., 35 (2000), pp. 87–109.
- [7] A. BERMUDEZ AND M. E. VÁZQUEZ, *Upwind methods for hyperbolic conservation laws with source terms*, Comput. & Fluids, 23 (1994), pp. 1049–1071.
- [8] L. CHEN, P. SUN, AND J. XU, *Optimal anisotropic meshes for minimizing interpolation errors in L^p -norm*, Math. Comp., to appear.
- [9] A. I. DELIS, *Improved application of the HLLC Riemann solver for the shallow water equations with source terms*, Comm. Numer. Methods Engrg., 19 (2003), pp. 59–83.
- [10] A. I. DELIS AND C. P. SKEELS, *TVD schemes for open channel flow*, Internat. J. Numer. Methods Fluids, 26 (1998), pp. 791–809.
- [11] A. I. DELIS AND TH. KATSAOUNIS, *Relaxation schemes for the shallow water equations*, Internat. J. Numer. Methods Fluids, 41 (2003), pp. 695–719.
- [12] R. FAZIO AND R. J. LEVEQUE, *Moving-mesh methods for one-dimensional hyperbolic problems using CLAWPACK*, Comput. Math. Appl., 45 (2003), pp. 273–298.
- [13] N. GOUTAL AND F. MAUREL, in Proceedings of the 2nd Workshop on Dam-Break Wave Simulation, HE-43/97/016/B, Département Laboratoire National d'Hydraulique, Groupe Hydraulique Fluviale Electricité de France, France, 1997.
- [14] A. HARTEN AND J. M. HYMAN, *Self adjusting grid methods for one-dimensional hyperbolic conservation laws*, J. Comput. Phys., 50 (1983), pp. 17–33.
- [15] C. HIRCH, *Numerical Computation of Internal and External Flows*, Wiley, New York, 1988.
- [16] M. E. HUBBARD AND P. GARCIA-NAVARRO, *Flux difference splitting and the balancing of source terms and flux gradients*, J. Comput. Phys., 165 (2000), pp. 89–125.
- [17] J. M. HYMAN, S. LI, AND L. PETZOLD, *An adaptive moving mesh method with static rezoning for partial differential equations*, Comput. Math. Appl., 10–11 (2003), pp. 1511–1524.
- [18] R. J. LEVEQUE, *Finite Volume Methods for Hyperbolic Problems*, Cambridge University Press, Cambridge, UK, 2002.
- [19] R. LI, T. TANG, AND P. ZHANG, *Moving mesh methods in multiple dimensions based on harmonic maps*, J. Comput. Phys., 170 (2001), pp. 562–588.
- [20] S. LI AND L. PETZOLD, *Moving mesh methods with upwind schemes for time dependent PDEs*, J. Comput. Phys., 131 (1997), pp. 368–377.
- [21] S. LI, L. PETZOLD, AND Y. REN, *Stability of moving mesh systems of partial differential equations*, SIAM J. Sci. Comput., 20 (1998), pp. 719–738.
- [22] S. V. PENNINGTON AND M. BERZINS, *New NAG software for first order partial differential equations*, ACM Trans. Math. Software, 20 (1994), pp. 63–99.
- [23] J. M. STOCKIE, J. A. MACKENZIE, AND R. D. RUSSEL, *A moving mesh method for one-dimensional hyperbolic conservation laws*, SIAM J. Sci. Comput., 22 (2001), pp. 1791–1813.
- [24] J. J. STOKER, *Water Waves*, Interscience, New York, 1957.
- [25] P. K. SWEBY, *High resolution schemes using flux limiters for hyperbolic conservation laws*, SIAM J. Numer. Anal., 21 (1984), pp. 995–1011.
- [26] E. TADMOR AND J. TANNER, *An adaptive order Godunov type central scheme*, in Hyperbolic Problems: Theory, Numerics, Applications, Proceedings of the 9th International Conference in Pasadena, 2002, T. Hou and E. Tadmor, eds., Springer-Verlag, Berlin, 2003, pp. 871–880.
- [27] Z. TAN, Z. ZHANG, Y. HUANG, AND T. TANG, *Moving mesh methods with locally varying time steps*, J. Comput. Phys., 35 (2004), pp. 17–33.
- [28] H. TANG, *Solution of the shallow-water equations using an adaptive moving mesh method*, Internat. J. Numer. Methods Fluids, 44 (2004), pp. 789–810.
- [29] H. TANG AND T. TANG, *Adaptive mesh methods for one- and two-dimensional hyperbolic conservation laws*, SIAM J. Numer. Anal., 41 (2003), pp. 487–515.
- [30] H. Z. TANG, T. TANG, AND P. W. ZHANG, *An adaptive mesh redistribution method for nonlinear Hamilton-Jacobi equations in two and three dimensions*, J. Comput. Phys., 188 (2003), pp. 543–572.